# Chiral Topological Defects in Nematic Liquid Crystals and Classical Field Theories

by

Brennan Douglas

An undergraduate thesis advised by Pavel Kornilovich

submitted to

Department of Physics, Oregon State University

in partial fulfillment of

the requirements for the

degree of

Baccalaureate of Science in Physics

Presented June 4th, 2019

Commencement June 2019

**ABSTRACT**

A great variety of topologically protected defects exist in ordinary and exotic states of matter. Some of them are promising candidates for technological applications such as magnetic memory or quantum computers. Others possess some properties of elementary particles that could lead to potential applications in quantum fields. Nematic liquid crystals provide a convenient platform to study the physics of such defects. A specific form of topological defects in nematics are ring disclinations. Here we studied this object in the form of a torus-shaped hole in the nematic field with a $\pi$-twist through the center. Vector models of liquid crystal energy cannot describe these objects as they lead to nonphysical discontinuities and spikes in energy density. Therefore, the tensor model of liquid crystals has been adopted for the energy model. An energy minimization algorithm was developed to calculate the minimum energy for a fixed torus size and free boundary conditions. The optimized defect energy was found to scale linearly with the torus size, in agreement with a scaling argument based on qualitative dimensional analysis. Potential relevance of ring disclinations beyond liquid crystals and specifically to classical field theories has been studied by including a fourth-order gradient term in the energy model. It was found that the optimized fourth-order configuration energy has a local minimum as a function of torus size. So, the global minimization path of the fourth-order energy model with respect to torus size was found and mapped.

**CONTENTS**

**LIST OF FIGURES**

## I. INTRODUCTION

A currently popular subject in physics is topology [1]. Topological defects have been found or proposed for many systems. These can span across many physical scales: nanometers for skyrmions in magnetic insulators, millimeters for vortices in superfluid helium, and cosmic distances for cosmic strings [2]. To further drive the point the 2016 Nobel Prize in Physics [3] was awarded for work involving topological phase transitions.

Topology exists in fields, so to study it one must have a system which is modeled by a field. Nematic liquid crystals (LC) are a state of matter that shares physical properties from traditional liquids and traditional solid crystals. This means that they can flow like liquids having no positional order while maintaining a long-range directional order. They provide a very convenient platform to study topology. Their state is characterized by a special vector field, the *director* [4]. The director field may include regions of discontinuity, defects, in the form of both points (*hedgehogs*) and lines (*disclinations*). These are defined by nonzero *topological charges*, meaning that they are topologically non-trivial. Some disclinations are open lines with their ends pinned to the walls of the container. Other disclinations are closed loops or event *knots*. This provides practically infinite topological variability to LCs.

LCs are stable at room temperature and ambient pressure. Powerful optical characterization methods exist for them — thanks to the massive investment put into them by the chemical and flat-panel display industries. This provides a large advantage to LCs experimentally. Due to this ease of use, a large number of complex topological defects have already been created and observed experimentally [5, 6].

The novelty that this work brings to the table is a special type of linear topological defect in nematic LC, the $q = 1/2$ *circular twist disclination*. It can be visualized and implemented by a torus — representing the circle — with the director going through the torus hole rotated by $\pi$ (see FIG. 1). This defect will be referred to as the $\pi$-twist. This twist is topologically stable unlike a similar twist with a $2\pi$ rotation. The $2\pi$-twist simply unwinds itself to a trivial configuration during the process of energy minimization. The $\pi$-twist could potentially be

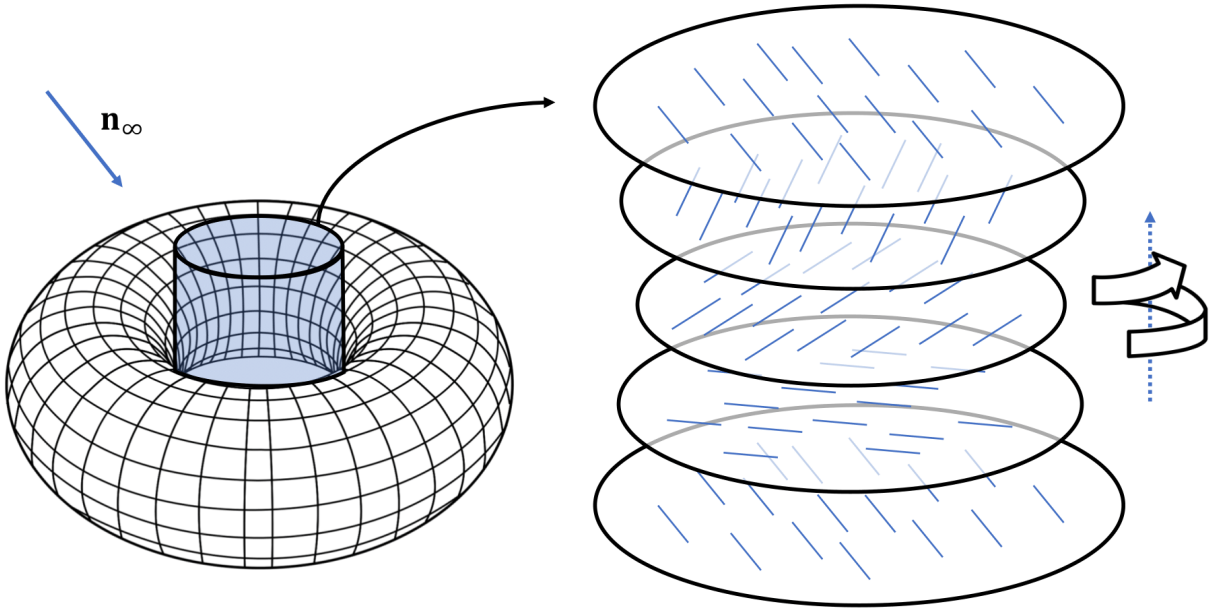


FIG. 1: $\pi$-twist torus configuration [7]. The torus [8] on the left represents the hole in the liquid crystal field. The liquid crystal field (represented by the blue lines on the right) is constant (with the top and bottom disks on the right and $\mathbf{n}_\infty$) everywhere that is not the blue cylinder. The slices on the right show the liquid crystal orientations through the center of the torus, they complete a $\pi$ rotation from bottom to top.

observed experimentally by mixing toroidal microparticles into a nematic LC and observing the nematic configurations in the tori centers. But it has not been done yet.

The complexities that the $\pi$-twist adds to the LC model are potentially why is has yet to be studied computationally. The $\pi$-twist has a natural discontinuity surface at which the director jumps 180 degrees (see FIG. 2). At this surface the field gradients report nonphysical singularities blowing up the traditional model's energy functional. Because of this issue the $\pi$-twist cannot be effectively simulated with the conventional vector models of LC energy that involves gradients of vector components. To overcome this the more complex and complete *tensor* model of the LC elastic energy was adopted, which is rarely used elsewhere [9].

An interesting application for twist topological defects is their theoretical use in classical field theories as models for elementary particles. The earliest proposal of that kind goes back to Larmor [10] who proposed that a twist in the aether can describe the just discovered electron. Though the idea of the classic aether has long since been discarded, in modern times

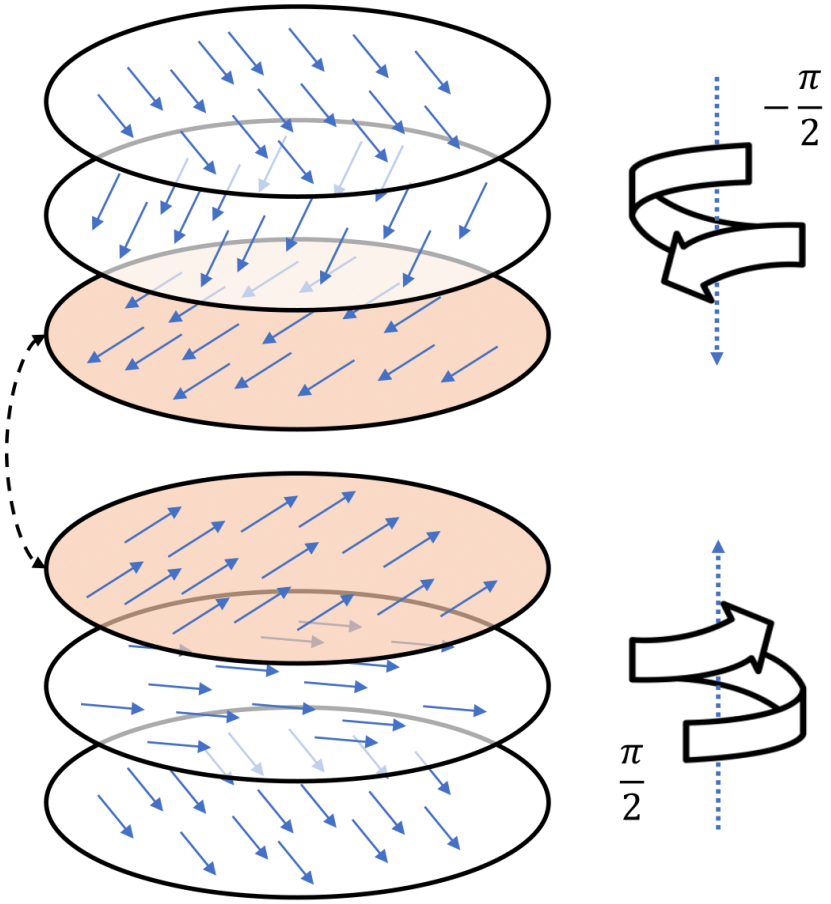


FIG. 2: $\pi$-twist discontinuity surface [7]. This shows the internal twist through the torus with the vector representation. The slices are divided into the top and lower half. The two shaded slices represent the same slice, just approached from the top for the top one and the bottom for the bottom. The vectors point in opposite directions, thus creating a discontinuity. This discontinuity creates a nonphysical delta function spike when the gradient of the field is calculated.

this idea prevails with Unzicker in an unpublished work [11]. Both of these proposals were formulated within the more conventional isotropic elastic theory, opposed to LC elasticity. And neither specifically mentioned the $\pi$-twist.

In more mainstream science, a related field-theoretical model is presented by Skyrme and Faddeev [12–14]. This model contains *nonsingular* topologically non-trivial solution called *Hopfions* [6]. The Skyrme-Faddeev model is believed to describe gluon complexes of quantum chromodynamics at low energy. The feature of the Skyrme-Faddeev model that is important to this work is the fourth-order gradient term. This term prevents Hopfions from collapsing

to a point. We take this concept and apply a simpler version of the Skyrme-Faddeev model to stabilize and prevent a similar collapse for the $\pi$-twist. This gave an avenue to explore what would happen when the torus could "change shape". Not directly, but through energy minimization (e.g. finding the energy minimum with respect to torus size across multiple field minimizations of a static torus).

A common challenge in modeling such systems is visualizing configurations. The present work was motivated in part by the lack of effective visualization methods for vector fields in three dimensions. Some experimental animations were developed to add more dimensions that could be used to display more information about the field.

### A. Outline

This paper has been set up to walk through our experience of expanding and exploring the theory and then the methods that were used to simulate the configuration. Section II covers the different physical models that were combined to create the final simulation. Simplifications were applied along the way to bring the computational aspect of the project into a reasonable scope.

Next, section III discusses the specific numeric techniques implemented in the simulation of the theory. The discontinuity added to the field, by the absence of field inside the torus, created complexities that needed to be carefully handled. Different aspects of the theory and qualitative estimates were used to test whether the simulation was producing accurate results that aligned with the theory.

In section IV we discuss some experimental visualization techniques that were worked on to help visualize the torus configuration. Even though the final field configurations for this work is simple and easy to understand, more complex defects quickly become too complicated to understand traditionally. To try and help solve this different animated methods were used.

In section V the final results yielded some insights about the torus defect. Specially, that the additional fourth-order term stabilized it within one dimension but not the other. As

its energy was minimized the torus tended to grow larger as it consumed more of the field, thus reducing its overall energy.

Finally, the appendix contains a list of much more extended theoretical derivations that were referenced throughout section II.

## II. PHYSICAL MODELS

### A. Classical Frank-Oseen elastic energy

The classical Frank-Oseen elastic energy model [4] for nematic liquid crystals describes their energy density:

$$f = \frac{1}{2} K_1 \left(\nabla \mathbf{n}\right)^2 + \frac{1}{2} K_2 \left(\mathbf{n} \cdot \left[\nabla \times \mathbf{n}\right]\right)^2 + \frac{1}{2} K_3 \left[\mathbf{n} \times \left[\nabla \times \mathbf{n}\right]\right]^2 \ , \tag{1}$$

where the $\mathbf{n}$ is the director field with the constraint $\mathbf{n}^2 = 1$.

At each point in the liquid crystal there are three different distortions that add to the energy density. These additions are represented, and scaled, by the three $K$ factors: $K_1$ corresponds to splay, $K_2$ to bend, and $K_3$ to twist. These different distortions in their isolated state can be observed in FIG. 3.

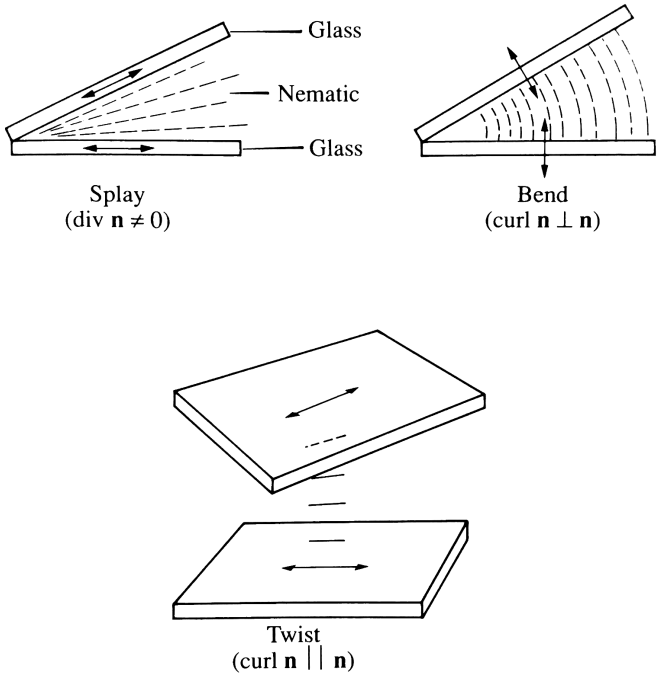


FIG. 3: Isolated energy field distortions for $K_1$, $K_2$, and $K_3$ components in (1) [4]. $K_1$ is the only active energy term from (1) in the splay (top left) field. $K_2$ is the only active energy term in the bend (top right) field. And $K_3$ is the only active energy term in the twist (bottom) field.

A key feature of the model is that the nematic liquid crystals are represented by unit length vectors $\mathbf{n}^2(\mathbf{r}) = 1$ at any non-singular point $\mathbf{r}$ of 3d space. This means that any change to $\mathbf{n}$ is pure rotation and $\mathbf{n}$'s magnitude is always unit length.

If a given field has any of these distortions — as defined in (1) — this means that the total energy of the liquid crystal field is in a heightened energy state. The total energy is a functional of the director field,

$$F[\mathbf{n}] = \int \mathrm{d}^3\mathbf{r} f, \tag{2}$$

subjected to particular boundary conditions of $\mathbf{n}$. This also implies that given a specific initial configuration for any liquid crystal field there will be a minimum energy state where these distortions are minimized.

When finding the minimal energy configuration a key constraint is the unit length of the liquid crystals. Thus, minimization of $F$ must be done within a subset of configurations with $\mathbf{n}^2 = 1$. This can be accomplished, for example, by parameterizing $\mathbf{n}$ with two polar angles $\theta$ and $\varphi$, then minimizing with respect to $\theta$ and $\varphi$. However, this leads to difficult non-linear differential equations. It is easier to apply the method of Lagrange multipliers. According to this method, instead of the *constrained* energy $F$, one considers *unconstrained* energy $\tilde{F} = F - I$, where

$$I[\mathbf{n}(\mathbf{r}), \mu(\mathbf{r})] = \frac{1}{2}\int \mathrm{d}^3\mathbf{r}\, \mu(\mathbf{r}) \left\{\mathbf{n}^2(\mathbf{r}) - 1\right\} \ . \tag{3}$$

$\mu$ is an arbitrary function of $\mathbf{r}$ (the position vector) and the unconstrained distortion energy

$$\tilde{F} = F - I \tag{4}$$

$$\tilde{F}[\mathbf{n}(\mathbf{r}), \mu(\mathbf{r})] = \int \mathrm{d}^3\mathbf{r} \left\{ f - \frac{1}{2}\mu(\mathbf{r}) \left(n_x^2 + n_y^2 + n_z^2 - 1\right) \right\} , \tag{5}$$

is a functional of both $\mathbf{n}(\mathbf{r})$ and $\mu(\mathbf{r})$. At equilibrium, $\tilde{F}$ must be minimal with respect to variations of both $\mathbf{n}$ and $\mu$. Note the minimum with respect to $\mu(\mathbf{r})$ is equivalent to the

constraint $\mathbf{n}^2 = 1$.

In the following we derive a practical method of minimizing $\tilde{F}$ and $F$. The equilibrium condition for (4) and (5) is

$$\frac{\delta \tilde{F}}{\delta n_k} = 0 \,, \tag{6}$$

where $n_k$ is the $k^{th}$ component of n and $\delta$ refers to a functional derivative. Equation (6) defines the minimum point for the unconstrained distortion energy. By applying (6) along with (4) the constrained distortion energy $F$ can be minimized. First, $\delta$ can be applied to (4),

$$\delta \tilde{F} = \delta F - \delta I = \delta F - \left\{ I\left[\mathbf{n} + \delta \mathbf{n}\right] - I\left[\mathbf{n}\right] \right\} \,. \tag{7}$$

Then $I$ with variation can be expanded while dropping quadratic terms of $\delta\mathbf{n}$ as they are small,

$$I\left[\mathbf{n} + \delta \mathbf{n}\right] = I\left[\mathbf{n}\right] + \int \mathrm{d}^3\mathbf{r} \left\{ \mu(\mathbf{r}) \left( n_x \delta n_x + n_y \delta n_y + n_z \delta n_z \right) \right\} \,. \tag{8}$$

This expression can then be substituted into (7),

$$\delta \tilde{F}\left[\mathbf{n} + \delta \mathbf{n}\right] = \delta F\left[\mathbf{n}\right] - \int \mathrm{d}^3\mathbf{r} \left\{ \mu(\mathbf{r}) \left( n_x \delta n_x + n_y \delta n_y + n_z \delta n_z \right) \right\} \,. \tag{9}$$

Finally, the functional derivative of (9) with respect to $\delta n_k$ can be taken while using (6),

$$0 = \frac{\delta F}{\delta n_k} - \mu(\mathbf{r}) n_k \,. \tag{10}$$

The first term in (10) defines the *molecular field*

$$h_k \equiv -\frac{\delta F}{\delta n_k} \,. \tag{11}$$

In principle, $h_k$ can be computed for any $\mathbf{n}$ if the energy model such as (1) is specified. Thus,

at equilibrium, the director $\mathbf{n}$ *must be parallel* to the molecular field $\mathbf{h}$

$$\mu\left(\mathbf{r}\right) n_k = -h_k = \frac{\delta F}{\delta n_k} \, . \tag{12}$$

Away from equilibrium, the last fact can be utilized to develop a relaxation algorithm: if $\mathbf{h}$ and $\mathbf{n}$ are not parallel, there exists a torque,

$$\mathbf{M} = \left[\mathbf{n} \times \mathbf{h}\right] \, , \tag{13}$$

that is trying to align $\mathbf{n}$ in the direction of $\mathbf{h}$. The optimization process can be thought as relaxation in *fictitious* time $t$, with a characteristic time scale $\frac{1}{\beta}$,

$$\frac{d\mathbf{n}}{dt} = \beta \left[\mathbf{M} \times \mathbf{n}\right] \, . \tag{14}$$

If the resulting torque is scaled down sufficiently small by $\beta$, the result of its addition to the original $\mathbf{n}$ would be that of a small rotation in the direction of $\mathbf{h}$. As $\mathbf{n}$ is changing, $\mathbf{h}$ is changing too. Thus, $\mathbf{h}$ must be recomputed at every step. If this action were iteratively applied to $\mathbf{n}$, across fictitious time, $\mathbf{n}$ would relax into the direction of $\mathbf{h}$. Once all of $\mathbf{n}$ is pointing in the direction of $\mathbf{h}$ at every point $\mathbf{r}$ the resulting vectors of the cross products from (13) will be zero and the field will no longer move. In summary, this leaves the change in direction of $\mathbf{n}$ with respect to fictitious time as,

$$\frac{d\mathbf{n}}{dt} = \beta \, \left[\left[\mathbf{n} \times \mathbf{h}\right] \times \mathbf{n}\right] \, . \tag{15}$$

One important note about the molecular field $\mathbf{h}$. The component of $\mathbf{h}$ parallel to $\mathbf{n}$ does not affect relaxation dynamics of $\mathbf{n}$. Furthermore, it has no physical meaning.

### B. One-constant approximation

The general method described previously is complex can get time consuming very fast. To reduce its complexity a simple and commonly made simplifying approximation is used,

$$K = K_1 = K_2 = K_3 \,. \tag{16}$$

In this *one-constant* approximation the Frank energy simplifies to

$$f_0 = \frac{1}{2} K \left\{ (\nabla \mathbf{n})^2 + [\nabla \times \mathbf{n}]^2 \right\} \,. \tag{17}$$

See appendix A 1 for the full derivation. This can be further simplified to (see appendix A 2),

$$f_0 = \frac{1}{2} K \sum_{i\,j=1,2,3} (\nabla_j n_i \nabla_j n_i) = \frac{1}{2} K (\nabla_j n_i \nabla_j n_i) \tag{18}$$

where $\nabla_1 = \frac{\partial}{\partial x}$, $\nabla_2 = \frac{\partial}{\partial y}$, and $\nabla_3 = \frac{\partial}{\partial z}$. Here Einstein notation summation rule is adopted to simplify the notation. A sum across indices is assumed whenever a single term has repeated indices that are not previously defined.

Next, the molecular field from (11) needs to be found given the specific energy function in (18). To solve for component $k$ of $F$ a small variation must be applied to $F$,

$$F[\mathbf{n}] \to F[\mathbf{n} + \delta\mathbf{n}] \,. \tag{19}$$

Then this is applied to the component form of $F$ and the squared components of $\delta n_k$ are dropped due to their smallness. It is found that $F[\mathbf{n}]$ can be extracted leaving,

$$F[\mathbf{n} + \delta\mathbf{n}] = F[\mathbf{n}] + K \int \mathrm{d}^3\mathbf{r}\, \nabla_i \mathbf{n} \nabla_i \delta\mathbf{n} \,. \tag{20}$$

Moving forward requires separating out $\delta n_k$, so integration by parts is performed,

$$\delta F = F\left[\mathbf{n} + \delta\mathbf{n}\right] - F\left[\mathbf{n}\right] \tag{21}$$

$$\delta F = K\left\{\delta n_k \nabla n_k - \int \mathrm{d}^3\mathbf{r}\, \delta n_k \nabla_i \nabla_i n_k\right\} . \tag{22}$$

At the boundaries of the region $\delta n_k = 0$

$$\delta F = -K \int \mathrm{d}^3\mathbf{r}\, \delta n_k \nabla_i \nabla_i n_k . \tag{23}$$

Pulling from (11), $h_k$ can be calculated,

$$h_k = -\frac{\delta F}{\delta n_k} = K \nabla_i \nabla_i n_k . \tag{24}$$

It is clear from this equation that each component of $\mathbf{h}$ is only dependent on its respective component in $\mathbf{n}$. This then makes it easy to holistically define $\mathbf{h}$ in its vectorial form to be,

$$\mathbf{h} = K\left(\nabla_i \nabla_i\, \mathbf{n}\right) . \tag{25}$$

### C. Tensor formulation

The vectorial formulation is sufficient for most cases, however it presents a flaw that fails to capture the entirety of the liquid crystals. The nematic liquid crystals are lines and not arrows, unlike vectors, this is stated as $\mathbf{n} \leftrightarrow -\mathbf{n}$. This presents the problem where there are two vectors parallel yet facing opposite directions. This is a continuous situation for the liquid crystals and discontinuous for the vector field. Simply, the liquid crystals have $\mathbf{n} \leftrightarrow -\mathbf{n}$ equivalence. This issue is relevant to this work as it focuses on the $\pi$-twist which creates this situation on one end of itself.

The solution is to rewrite the model using tensors which are bi-linear combinations of vector components [9]. So, some basic tensor notation needs to be introduced. The symmetrical

tensor $Q_{jk}$ is defined as

$$Q_{jk} = n_j n_k - \frac{1}{3}\,\delta_{jk}\,. \tag{26}$$

Through the derivation in appendix (B 1) — which follows Tu et al [9] — it is shown that (18) is equivalent to,

$$f_T = \frac{1}{4}\,K\,(\nabla_i Q_{jk}\,\nabla_i Q_{jk})\ . \tag{27}$$

This simple equation looks harmless, however beneath the Einstein summation is a hidden triple sum. When expanded this comes out to 27 terms.

The corresponding molecular field for the tensor model is also found following Tu et al [9]. The derivation can be found in the appendix (B 2),

$$h_k = K\,n_j \nabla_i \nabla_i\,Q_{jk}\,. \tag{28}$$

Expanded into components, the molecular field is:

$$h_1 = K\left(n_1\nabla_i^2 Q_{11} + n_2\nabla_i^2 Q_{12} + n_3\nabla_i^2 Q_{13}\right), \tag{29}$$

$$h_2 = K\left(n_1\nabla_i^2 Q_{12} + n_2\nabla_i^2 Q_{22} + n_3\nabla_i^2 Q_{23}\right), \tag{30}$$

$$h_3 = K\left(n_1\nabla_i^2 Q_{13} + n_2\nabla_i^2 Q_{23} + n_3\nabla_i^2 Q_{33}\right). \tag{31}$$

The advantage of (29)-(31) over vectorial counterparts (18) and (25) is that the basic object $Q_{jk}$ is invariant under $\mathbf{n} \leftrightarrow -\mathbf{n}$, and therefore is continuous across the discontinuity surface (FIG. 2). Therefore, gradients $\nabla_i Q_{jk}$ are well-defined everywhere. With the molecular field defined in (29)-(31) the relaxation procedure (15) can now be implemented.

### D. A fourth-order gradient model

As the model currently stands the energy of the torus decreases with its volume. This configuration cannot ever exist within liquid crystals by itself without toroidal particles. This can be seen by looking at the scaling of the energy density and total energy. The

approximate size of the derivatives are $\nabla_i n_k \sim \frac{1}{R}$, where $R$ are is the characteristic width of the torus defect. This can then be applied to the energy density,

$$f \sim (\nabla_i n_k)^2 \sim \frac{1}{R^2} \,. \tag{32}$$

Then the approximate size of the total energy is

$$F = \int f dV \sim f R^3 \sim \frac{1}{R^2} R^3 = R \,. \tag{33}$$

This shows that the larger a defect in the LC field the larger the energy. So, if given the chance the field will reduce the size of defects to reduce its overall energy. To solve this problem a transition from the physical liquid crystals to the classical field theory needs to be made, a fourth-order term can be added.

Adding a fourth-order term would balance out this energy scaling. Consider the same scaling of this term as above,

$$f_4 \sim (\nabla_i n_k)^4 \sim \frac{1}{R^4} \,. \tag{34}$$

Now calculate the scaling of the total energy due to this forth order term,

$$F_4 = \int f_4 dV \sim f_4 R^3 \sim \frac{1}{R^4} R^3 = \frac{1}{R} \,. \tag{35}$$

Notice that the $\frac{1}{R}$ does the opposite of the standard energy $F$. To reduce energy, it makes the defect larger. Now, combine $F$ and $F_4$ to find the total energy with the forth order term added on,

$$F_{Total} = c_1 R + c_2 \frac{1}{R} \tag{36}$$

where $c_1$ and $c_2$ are just constants. These two terms will balance each other out to create a

minimum energy point, thus allowing the torus to be stable without toroidal particles.

There is a widely accepted fourth-order gradient energy equation that allows for stable knots, configuration with non-trivial topology, to form in the absence of an internal surface, the Faddeev-Skyrmec model [12]. Traditionally, it is formulated in terms of vectors as the configurations it was designed for are continuous. Its energy density reads,

$$f_{SF} = \frac{K}{2}\frac{\partial n_i}{\partial x_j}\frac{\partial n_i}{\partial x_j} + \frac{g}{4}\left\{\vec{n}\cdot\left(\frac{\partial \vec{n}}{\partial x_i}\times\frac{\partial \vec{n}}{\partial x_j}\right)\right\}^2 . \tag{37}$$

Note that the first term coincides with the LC elastic energy in the one-constant approximation (18). However, the second term has a complicated structure. The key aspect of this additional term is the fourth-order gradients.

By using the rules of tensor algebra, one can show that the fourth-order term in (37) can also be written as

$$\left\{\vec{n}\cdot\left(\frac{\partial \vec{n}}{\partial x_i}\times\frac{\partial \vec{n}}{\partial x_j}\right)\right\}^2 = \left(\frac{\partial n_k}{\partial x_i}\frac{\partial n_k}{\partial x_i}\right)\left(\frac{\partial n_p}{\partial x_j}\frac{\partial n_p}{\partial x_j}\right) - \left(\frac{\partial n_k}{\partial x_i}\frac{\partial n_k}{\partial x_j}\right)\left(\frac{\partial n_p}{\partial x_i}\frac{\partial n_p}{\partial x_j}\right) . \tag{38}$$

Take note of the absurd size of the second term. It is a quadruple sum, where each index has 3 possible values. Both these terms expand into 81 parts.

By comparing (18) and (38) it is noticed that the first term in (38) is just the square of the first term in (18). Thus, to simplify the computational task we retain only the first term in (38). In the original Skyrme-Faddeev model the second term in (38) is needed to stabilize topologically nontrivial Hopfions. In the present model, the nontrivial topology is stabilized by the presence of the torus, and additional "help" is not needed. Thus, the omission of the second term does not change the physics we care about here. At the same time, being of the fourth-order, the first term alone is sufficient to prevent torus collapse (see energy scaling argument at the beginning of this section). Thus, our full model is,

$$f_4 = \frac{K}{2}\frac{\partial n_i}{\partial x_j}\frac{\partial n_i}{\partial x_j} + \frac{g}{4}\left(\frac{\partial n_k}{\partial x_i}\frac{\partial n_k}{\partial x_i}\right)\left(\frac{\partial n_p}{\partial x_j}\frac{\partial n_p}{\partial x_j}\right), \tag{39}$$

or, in tensor terms

$$f_{4T} = \frac{1}{4} K \left( \nabla_i Q_{jk} \, \nabla_i Q_{jk} \right) + \frac{1}{16} g \left( \nabla_i Q_{jk} \, \nabla_i Q_{jk} \right)^2 \tag{40}$$

with a standard total energy of

$$F_{4T} \left[ Q_{ik} \right] = \int d^3 \mathbf{r} \left\{ f_{4T} \right\} \ . \tag{41}$$

Now that there are two constants their relationship matters. To simplify the numerics $F_{4T}$ can be non-dimensionalized. First note the constants' dimensions,

$$[K] = \frac{J}{m} \tag{42}$$

$$[g] = Jm \, . \tag{43}$$

From these dimensions a length unit can be constructed,

$$\lambda = \sqrt{\frac{g}{K}} \, , \tag{44}$$

and an energy unit can be constructed,

$$\epsilon = \sqrt{Kg} \, . \tag{45}$$

With the length unit new dimensionless position coordinates can be defined,

$$\xi = \frac{x}{\lambda} \ , \ \upsilon = \frac{y}{\lambda} \ , \ \zeta = \frac{z}{\lambda} \, . \tag{46}$$

A change of coordinates is applied to $f_{4T}$. These new coordinates will be expressed in the same index as before with a prime on their indices. First, the first derivatives of $\mathbf{n}$,

$$\nabla_i \mathbf{n} = \frac{1}{\lambda} \nabla_{i'} \mathbf{n} \, . \tag{47}$$

Then the change of variables can be applied to the total energy (41),

$$\begin{aligned} F_{4T} &= \int d\xi d\upsilon d\zeta \left\{\lambda^3 f_{4T}\right\} \\ &= \int d^3\mathbf{r}' \left\{\lambda^3 f_{4T}\right\} \\ &= \int d^3\mathbf{r}' \left\{\lambda^3 \left[\frac{K}{\lambda^2}\left(Q_{j'k',i'}\, Q_{j'k',i'}\right) + \frac{g}{\lambda^4}\left(Q_{j'k',i'}\, Q_{j'k',i'}\right)^2\right]\right\} \\ &= \int d^3\mathbf{r}' \left\{K\lambda\left(Q_{j'k',i'}\, Q_{j'k',i'}\right) + \frac{g}{\lambda}\left(Q_{j'k',i'}\, Q_{j'k',i'}\right)^2\right\} . \end{aligned} \tag{48}$$

The coefficients to the energy terms in (48) are left as $K\lambda$ and $\frac{g}{\lambda}$. These can be simplified using the unit definition for $\lambda$ from (44) to

$$K\lambda = K\sqrt{\tfrac{g}{K}} = \sqrt{Kg} \;=\; \epsilon \tag{49}$$

$$\frac{g}{\lambda} \;= g\sqrt{\tfrac{K}{g}} = \;\sqrt{Kg} \;=\; \epsilon\,. \tag{50}$$

Notice that they are both equal and equivalent to $\epsilon$ as per its definition from (45). This leaves the total energy as (new coordinate system implied),

$$F_{4T} = \epsilon \int d^3\mathbf{r}' \left\{\left(\nabla_i Q_{jk}\, \nabla_i Q_{jk}\right) + \left(\nabla_i Q_{jk}\, \nabla_i Q_{jk}\right)^2\right\} . \tag{51}$$

This allows the simulation to calculate energy in units of $\epsilon$ with no coefficients to worry about. As there are no parameters left this simplifies the numerical work, the minimum energy with respect to them is not a consideration.

### E. Boundary conditions

There are two boundaries in the LC, the edges of the simulation and the surface of the torus. The edges of the simulation are simple to set. As the defect is localized around the torus it is known that the further away the field is from the torus the more it approaches the infinity direction $\mathbf{n}_\infty$, the standard (global) direction of the field (e.g. $\mathbf{n}_\infty = \mathbf{k}$ or $\mathbf{n}_\infty = \mathbf{i}$). Because this is known to be constant the simulation boundary edges are held to be constant

at $\mathbf{n}_\infty$. So, they are never updated during the simulation, they are strongly anchored.

The surface of the torus is the opposite (by design), it is weakly anchored. This means that the directors $\mathbf{n}$ next to the surface of the torus are free to rotate in any direction they like. This allows the topology of the field to take precedence over the torus itself. It also reduces the computational scope as now different configurations on the surface of the torus do not need to be analyzed or considered.

During development of the simulation it was found that the second derivatives at the boundaries (non-symmetric second derivatives) were unstable. This wasn't an issue at $\mathbf{n}_\infty$ as those are strongly anchored and never updated. However, for the weak anchored boundary conditions at the torus surface this proved an issue. The solution was to hold them strongly anchored for small intervals ($\sim 5$ iterations) then average them with their neighbor nodes as the field is small enough to be considered continuous on this scale. This update process is highlighted in FIG. 8.

### F. Global rotation

There are two characteristic directions in the systems: torus axis $\mathbf{b}$, and the field at infinity $\mathbf{n}_\infty$. It can be shown that the energy is independent of the mutual orientation (angle) of $\mathbf{b}$ and $\mathbf{n}_\infty$, or, which is the same, that the energy is invariant under global rotations of either $\mathbf{b}$ or $\mathbf{n}_\infty$. This is an important factor to eliminate as it reduces the number of instances that need to be run, thus minimized the computational load. This is proved in detail at appendix C.

This was also tested numerically as it was an indicator that could be used to test whether our implementation was correct. A sphere grid was created, and the configuration was run through the minimization code for each of the infinity directions from the sphere grid. The minimum energy was found to be constant through all the runs.

## III. NUMERICAL METHODS

### A. Field rasterization

One large issue is that these configurations are far too complex to minimize analytically. So, a numeric approach was taken instead. The nematic liquid crystal vector field can be discretized down to a grid. So, there will be three arrays, one to hold each component of the vectors. The simple operations, such as adding and subtracting, are trivial with this set up. However, derivatives and integrals need to have a closer look taken.

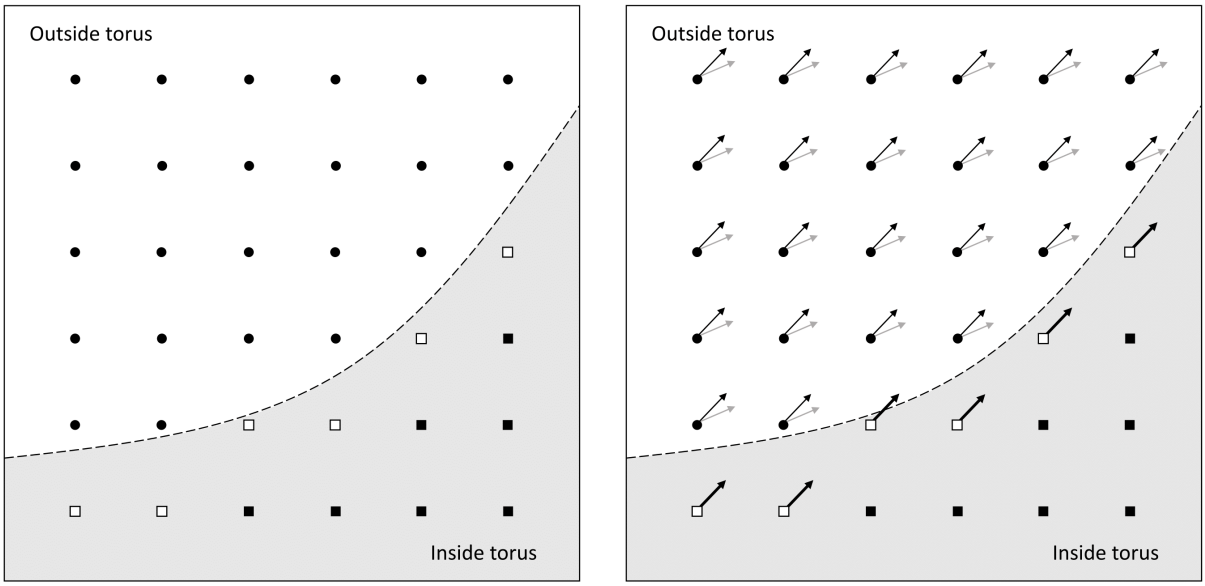


(a) Node classifications with respect to the torus surface

(b) Iteration update procedure per node classification

FIG. 4: Surface boundary conditions and iteration procedure. The gray area on the graph represents the empty portion of the field inside the torus surface (given by the dashed line). (a) shows the three classifications of nodes around the internal torus surface. Outside of the surface are the bulk field points, these are represented by black circles. Nodes both inside the surface and with neighbors outside the surface are kept separate for integration and second derivative calculations, these are represented by white squares. Finally, the nodes completely inside of the surface (where there is no field) are represented with black squares. Then (b) shows the update procedure during the minimization process. The bulk points (black circles) are always updated every iteration. However, the inside surface points (white squares) still represent field but are calculated by averaging the values at their neighbors every $m$ iterations.

### B. Derivatives

Derivatives will be tackled by using the finite difference between the closest points and dividing that by the width across which it spans. This will approximate what the derivative is. This finite difference method also has the added benefit of increasing in accuracy as the distance between the points decreases (e.g. the continuous limit). There are three forms of this finite difference: forward, backward, and center. The forward derivative only considers the point at which the derivative is being taken and the point *in front of it*, meaning the positive direction. For a function $f(x)$ discretized with grid width $a$ the forward finite difference is,

$$\frac{\partial f}{\partial x} \approx \frac{f(x+a) - f(x)}{a} \,. \tag{52}$$

Conversely, the backward finite difference is,

$$\frac{\partial f}{\partial x} \approx \frac{f(x) - f(x-a)}{a} \,. \tag{53}$$

Where the backward finite difference is just the opposite of the forward finite difference. Both of these are valid is some cases. However, they can vary from each other quite drastically at times. One prime example would be the maximum point of a sharp function (respective to the grid width).

This can be solved by using the points on both sides. The symmetric finite difference creates a secant line that approximates the tangent line at the point. As the grid width decreases and the points get closer together it becomes a closer and closer approximation. In equation form,

$$\frac{\partial f}{\partial x} \approx \frac{f(x+a) - f(x-a)}{2a} \,. \tag{54}$$

All these different forms of the first order finite differences are important to the simulation as the boundary cases where there is no data (e.g. the edge and internal surfaces) still need to be calculated and handled.

These different types of finite differences exist for the second order as well. However,

they are not needed as they produce much more unstable results (e.g. the forward second finite difference is simply the symmetric second finite difference on the point in the forward direction). As the field is minimized using second order derivatives, these instabilities often produce nonphysical and unexpected results. To get around this the points at the internal surface of the torus (the only points where a non-symmetric second derivative needs to be applied) are *relaxed* by averaging the values of the neighbor points (discussed more in III E). An illustration of which points get updated during an iteration can be found in FIG. 4b.

All this being said, the symmetric second order finite difference is still used in the internal bulk of the field,

$$\frac{\partial^2 f}{\partial x^2} \approx \frac{f(x+a) - 2f(x) + f(x-a)}{a^2} \,. \tag{55}$$

### C. Integration

On a grid, numerical integration over a volume is replaced with a finite sum over elementary cubes. Numeric integration of the grid is straightforward for continuous fields. Here the only boundaries of the field are the outside edges. Sum up all of the internal values (e.g. the energy density) and then add on half of the values of the boundary faces (this is because the wall cuts halfway through the volume *cube* the point describes), add on a quarter of the values where two boundaries meet, and finally add on an eighth of the values at the corners (e.g. where three boundaries meet). To finish off the numeric integration calculation, for a continuous field, multiply this final summation value by the grid width cubed, $a^3$.

The issue with this method comes when discontinuities are added to field. These are volumes where no field exists (e.g. inside of the torus that is being studied). This creates some internal nodes that are lacking one or more neighbors. Analytically this is a smooth surface cutting through a cube, numerically this can be represented as a fraction of the volume of each cube that is represented as a point. Once the fraction of existing field within each cube is known every node can be multiplied by their respective fraction, summed

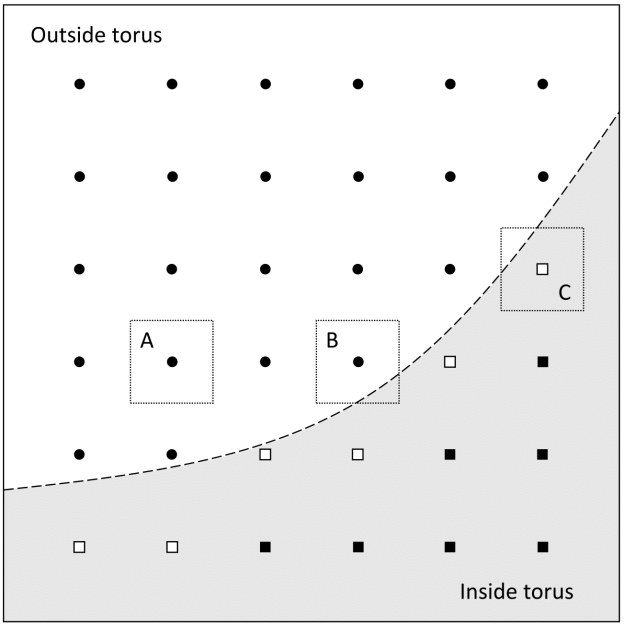


FIG. 5: 2D depiction of a grid cut with a smooth curve. The shaded section is where there is no field. The dashed line surrounding A is the area that node A represents. The nodes just on the inside of the curve (where there is no field), represented by hollow squares, still have values as they still have a portion within their area outside the curve. So, roughly in this depiction A has 100% active field, while B has 80% and C has 20%. These partial volumes for all the nodes are calculated once, in the beginning of the simulation.

together, and then multiplied by the width of the grid cubed, $a^3$.

The trick comes in calculating this volume fraction as it is possible for complex surfaces to be running through even a single cube as seen in the 2D representation of FIG. 5. Luckily as only the field is being minimized this boundary is static, so the fractions only need to be calculated once. So, at the beginning of the relaxation a much higher mesh is applied to each volume that each point represents — the 3D analog to A's dashed area in FIG. 5.

In this higher resolution mesh created around each point in the original grid, each point of the new mesh is assigned a one if it falls outside of the surface (outside of the torus) and a zero if it falls inside the surface (inside of the torus). The process of determining if a point falls inside or outside of the torus (surface) is discussed in III D. Then all the points' values are added together and divided by the total number of points. This produces a fraction for the original grid's point that the new mesh was centered on that represents the percentage of its volume that is part of the field — outside of the torus.

Now that the *partial volumes* for each point are calculated integration of the field can be accomplished. Before summing all of elements of the field (with the same parts of the boundaries removed) as before the value of each point is multiplied by its respective partial volume fraction. In this way, only the values of the field that is outside of the surface (torus) are added to the integral total.

The accuracy of this method was tested by using the computed fractions to calculate the total volume of both the inside of the torus and the outside volume surrounding the torus. These calculated values were then compared against the actual (theoretical) values given by the analytical representation of the torus and the volume. This method yielded a converging result the smaller the resolution got. So, as the resolution decreased towards zero the minimum energy converged to a finite value. This was a test that helped confirm the code correctly minimized the configuration in accordance with the theory.

### D. Torus surface

The representation of the torus in the grid is produced using an analytical representation of the torus volume with parameters $\tau$ and $u$,

$$\tau = \ln\left(\frac{\sqrt{\left(\sqrt{x^2+y^2}+u\right)^2+z^2}}{\sqrt{\left(\sqrt{x^2+y^2}-u\right)^2+z^2}}\right) . \tag{56}$$

Here $u$ is the other parameter that defines the shape of the torus (it is related to the width of the inner hole). For a single simulation $u$ is set to a constant value $u_0$. This equation allows for toroidal coordinate $\tau$ to be calculated for each point in the grid. The torus surface is then defined by $\tau = \tau_0$ where $\tau_0$ is a constant value (the constant lines of $\tau$ have been visualized in FIG. 6). Then the $\tau$ value for each point in the grid is compared to the torus', it is inside the torus if $\tau > \tau_0$ and outside the torus if $\tau < \tau_0$.

For a given $\tau_0$ and $u_0$ the volume of the torus is defined by,

$$V = \left(2\pi^2 u_0\right) \frac{\coth\ \tau_0}{\sinh^2\ \tau_0}\,. \tag{57}$$

Two other important values for the torus that were used during the simulation are the tube radius $r$ (the radius of the circular tube) and the inner radius $R$ (the distance from the center of the tube to the center of the torus),

$$r = \frac{u}{\sinh\ \tau_0} \tag{58}$$

$$R = u \cdot \coth\ \tau_0\,. \tag{59}$$

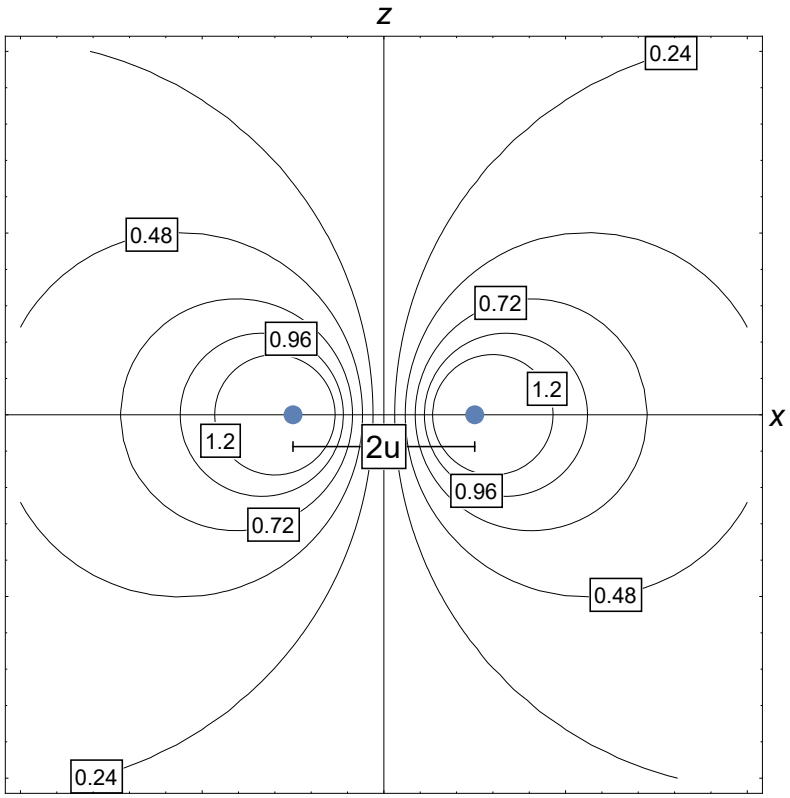


FIG. 6: Toroidal coordinates, contour lines of $\tau$. This shows how $\tau$ represents the shape of the torus itself. The second parameter $u$ can be seen effecting the width of the two foci (blue dots). If rotated around the $z$-axis a torus would form from each of the constant $\tau$ lines. As $\tau$ gets smaller the size of the torus increases, as it gets larger it collapses towards the two foci (the two dots on the $x$-axis).

When deciding the size of grid to run a certain torus shape on, the discrete width of the torus was calculated using $2R$. This entailed counting the number of nodes across both the width of the torus tube and the width of the torus. If either of these were too small (defined as 10 nodes across or less) the shape of the torus was distorted, and therefore was considered the minimum limit of the simulation. This metric helps define the balance between the resolution of the grid and the size of the torus.

On the other end of the balance spectrum it was important to check that the torus didn't go outside the bounds of the region being simulated. Clearly, this is not a system that can be analyzed as the torus is *cut* off at the region edge. The maximum torus size for a given region was defined to be when there are 10 or less nodes between the surface of the torus and the edge of region on any side.

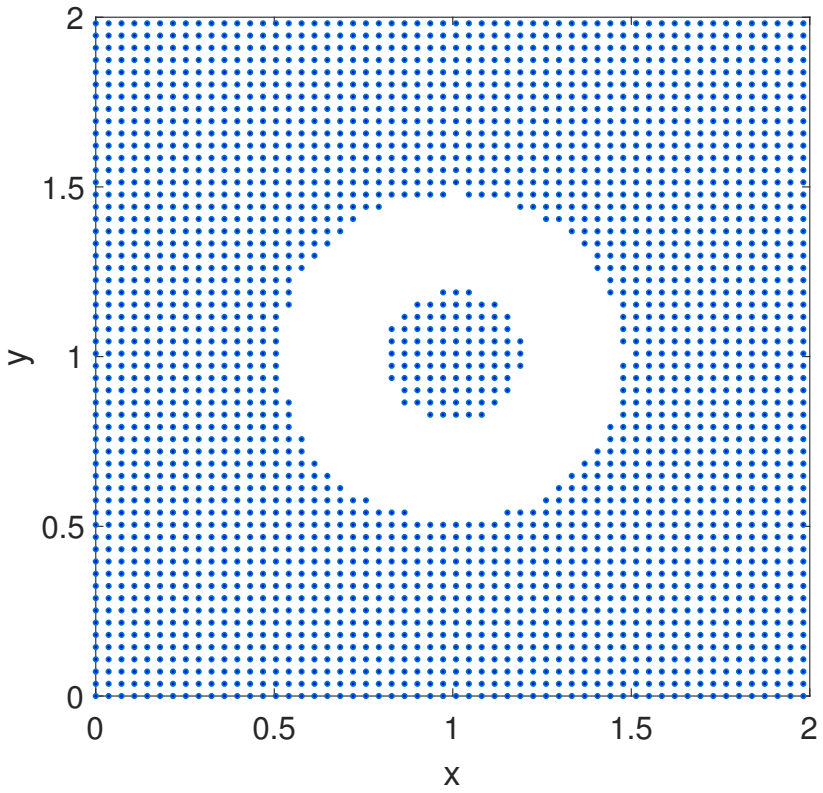


FIG. 7: Torus inside discretized grid. This shows how the torus surface is represented in the simulations discretized grid. A slice of the 3d space was taken at the midpoint on the $z$-axis. The white part without any points is the inside of the torus.

### 1. *Node classification*

The key aspect that the torus surface provides for the simulation is the ability to classify nodes in relation to the torus (see FIG. 4a). As previously stated, the surface of the torus is defined by $\tau = \tau_0$. The nodes outside the surface $\tau < \tau_0$ are nodes where the field value is stored and minimized. These nodes represent the LC field. The nodes inside the torus, $\tau > \tau_0$ have two separate classification: at the surface and the bulk of the torus. The surface nodes are the inside nodes that have a neighbor that is an outside node, all the others are the bulk nodes.

The surface nodes are important as their unit box still has some valid field inside of it (see FIG. 5). So, these nodes still hold a value for the field that is updated. They also play an important role in stabilizing the field minimization. As the inside torus surface nodes are the boundary between the bulk of the LC field (the outside nodes) and the bulk inside nodes this is where the second derivative becomes non-symmetric. The handling of non-symmetric second derivatives is further discussed in section III E.

## E. Boundary node relaxation

As mentioned previously, the non-symmetric second finite differences produced unstable results. As the second derivatives of the surface nodes within the region (those on the surface of the torus) still needed to be calculated another way was found. A fundamental assumption about the simulation is that the resolution of the grid is high enough that the field is continuous around a node (that is its neighbors have approximately the same value). This means that instead of directly calculating the second derivative that these edge nodes the value could be calculated by averaging their neighbors (FIG. 8).

One issue with this method is that our starting configuration might not be perfectly continuous and smooth at all points. To remedy this, the *relaxing* of the boundary nodes was not started until 100 iterations into the minimization of the field. This allows the initial condition to smooth out before the averaging begins. Another key factor is that the boundary

nodes were only relaxed every five iterations — once started. This allowed for substantial changes to occur within its neighbors while also reducing the computational load that the averaging added.

The consistency of this method was numerically confirmed by running many different tests with varied initial relaxing delay and iteration skip delays. Across these tests minimal deviation in the final minimum energy was observed. This leads the conclusion that these parameters did not affect the final energy.

### F. Initial configuration

An important aspect to the configuration of the simulation region is the "infinity" direction. This is the direction that the field points at the boundaries of the region. They represent the direction the field at infinity would possess.

The initial condition for the field's half-twist ($\pi$ rotation) through the center is completed

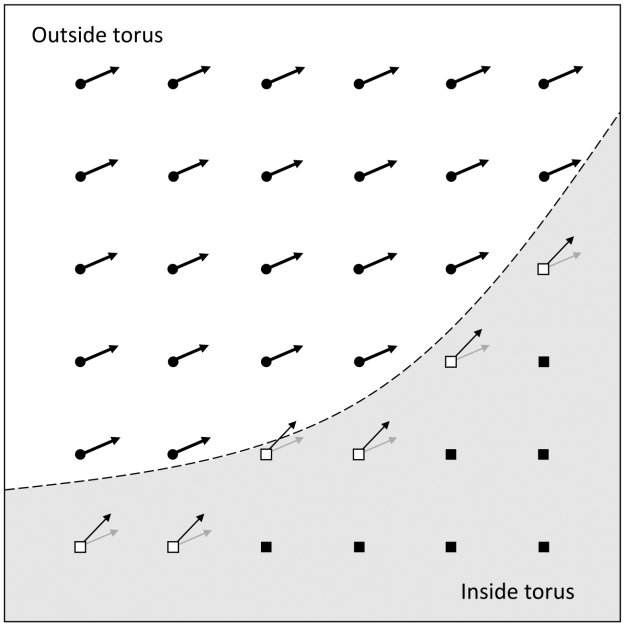


FIG. 8: Relaxation of surface boundary nodes. The nodes inside the torus surface that have neighbors outside of the surface and hold field values themselves (white squares) are updated separately from the bulk of the field (black circles). Every $m$ iterations their updated value is calculated by averaging their neighbors outside of the surface. Their new averaged values are represented by the grey arrows.

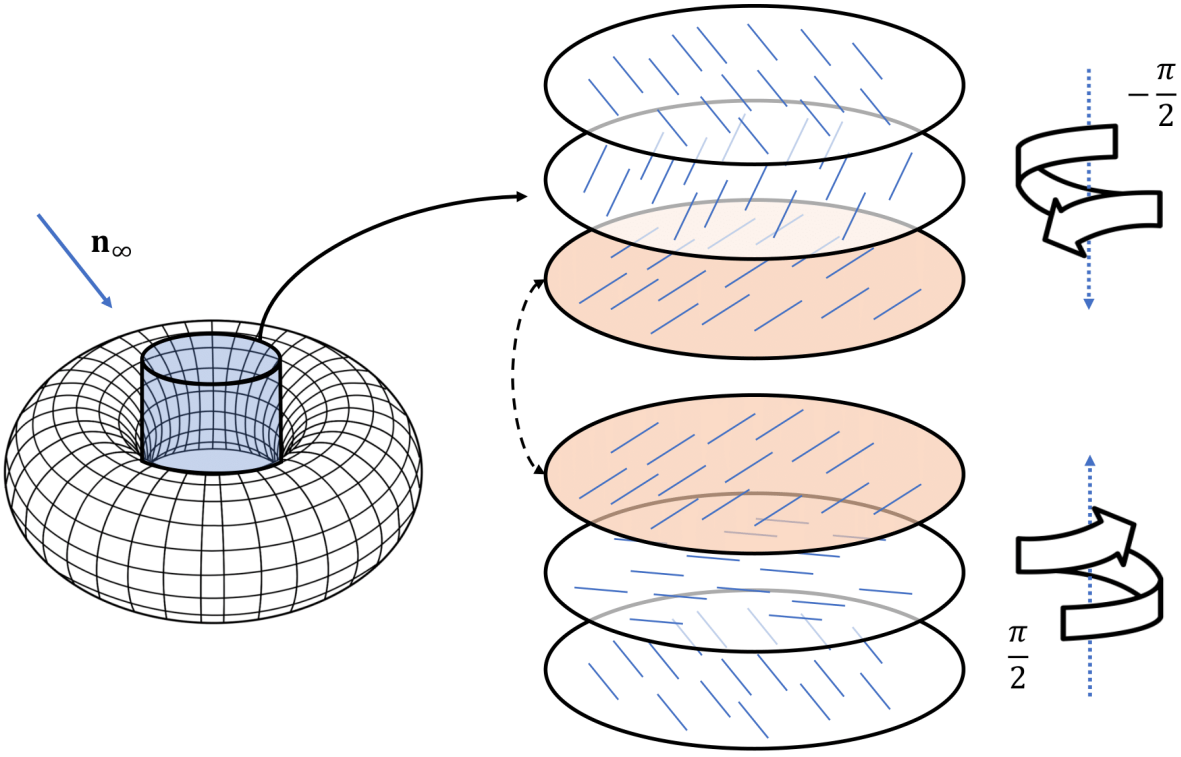


FIG. 9: Half twist initial configuration through the center of the torus [7]. The blue cylinder represents the size of the twist and the stack of disks represent slices of the liquid crystal inside of the cylinder. Both the top and bottom disks are in the direction of $\mathbf{n}_\infty$. The top half of twist rotates $-\frac{\pi}{2}$ to meet the bottom half of the twist, which has rotated $\frac{\pi}{2}$, at the *gluing* surface, represented by the shaded disks. The liquid crystal field completes a $\pi$ rotation in total through the height of the twist.

using a "twist region". In this region the field rotates along the plane created from the infinite direction and the normal vector of the plane created by the infinite direction and the $z$-axis (the torus axis). The rotation angle is with respect to the infinite direction. This allows the top and bottom regions of the field (split by the $xy$-plane through the center of the torus — the center line from FIG. 9) to twist in opposite directions and meet in the middle. In this way the natural symmetry of the system is preserved allowing for less concern about an unstable initial configuration. This is referred to as the *gluing* surface. At the gluing surface the nodes above it have a rotation of $-\frac{\pi}{2}$ (from the orientation at the boundaries) and the nodes below have $\frac{\pi}{2}$. The rotation angle is linearly interpolated along the $z$-axis from zero to its final value at the gluing surface.

At the boundaries of the twist region (the box from FIG. 9) there is a linear interpolation back to the bulk of the field. This is important to maintain the continuous nature of the field. All imperfections of the initial condition are smoothed out within the first 100 iterations of the minimization process. The crucial part is that the topology is set correctly so that the minimization will not unwind the twist.

### G. Simulation verification

Verification of the simulation was performed to prove that the methods aligned with the theory and that it was implemented correctly. This involved setting up a system where one variable could then be varied to see if the final minimum energy of the system was affected by these changes. These tests were carried out in MatLab, calling the simulation code with different inputs.

A key variable that was tested was the resolution of the grid. Starting from a reasonable grid resolution many higher resolutions were run, it was found that there was little variation in the minimum energy. As the grid approached an infinite resolution (continuous field) the minimum energy converged to a finite value (FIG. 10). This confirmed that the system was stable. Other variables that were tested were the start delay of the boundary node relaxation as well as the interval at which it relaxed, the height of the initial twist, and the global rotation of the director field (analogous to the rotation of the torus).

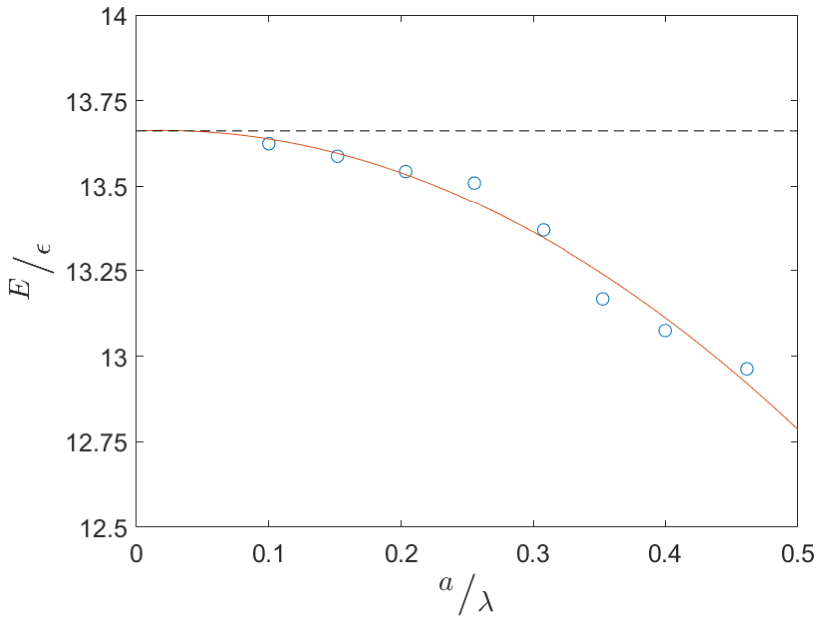


FIG. 10: Converging energy with high grid resolution. As the mesh resolution increases (grid width decreases, $a \to 0$) the energy converges to a finite value. The blue points were the simulation runs, then the red line was fit to their output and extrapolated to zero. Where this fit line intersected with the y-axis (dashed line) is the final value for a specific configuration, this represents a continuous field ($a = 0$).

## IV. VISUALIZATION OF VECTOR FIELDS

Visualizing complex 3D vector fields is a hard task. The default approach, a quiver plot (implemented in Matlab, for example), shows each vector's orientation at its point. This barely works for even low-density grids of points. Once the density of the grid becomes anything more than trivial the screen becomes a mess. Given the amount of information that is in these fields it becomes apparent that static images are lacking.

Visualization techniques become more important as the complexity of the field increases. With the torus the field is straightforward to think about and understand. There are still convenient and simple plans that can be sliced through at different levels to provide further understanding of how the field interacts with the torus. But, what if there were two tori, or instead of a torus it was an object with two holes. In these situations, the field will become more complex and there will no longer be simple planes to analyze. If there was a good way to display this information to make it more understandable these objects and systems would be far simpler to study.

A good candidate is animations, they provide a much larger number of dimensions to display aspects of the field. For 2D vector fields moving "tracers", objects with trails that stick to their path (potentially fading over time), provide an excellent view of the field. A superb example of this in action is a wind map for Earth (FIG. 11) [15]. Their heads follow the direction of the field and their tails show where they have been. When many of these are combined the patterns in the field emerge providing a clear image of how the field is composed. Time can also be used, their speed can be changed based off parameters of the field, potentially allowing for the magnitude of the field to be shown in this way – or another aspect of the field. The divergence of the field becomes amply apparent with tracers, they will either leave empty space or all converge on one point. Finally, color can be taken advantage of to display another attribute or to further highlight one again. In FIG. 11 [15] both the color and the speed of the animation represent the speed of the wind.

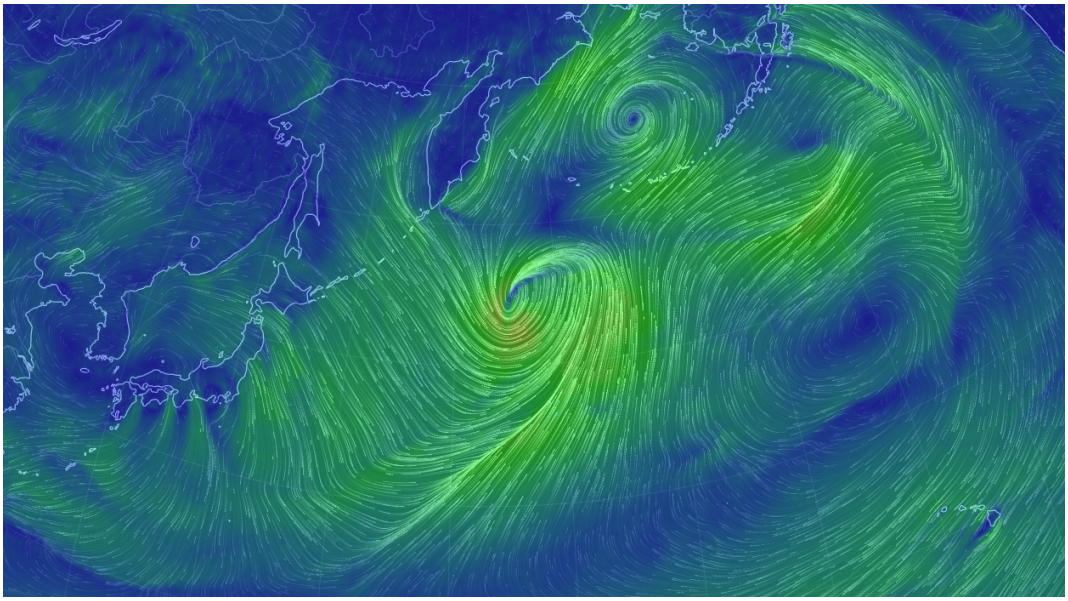

FIG. 11: Earth wind visualization [15]. This is an example of the 2D tracer method. Each of the lines are flowing in the direction of the wind, creating a strong visual representation of the field.

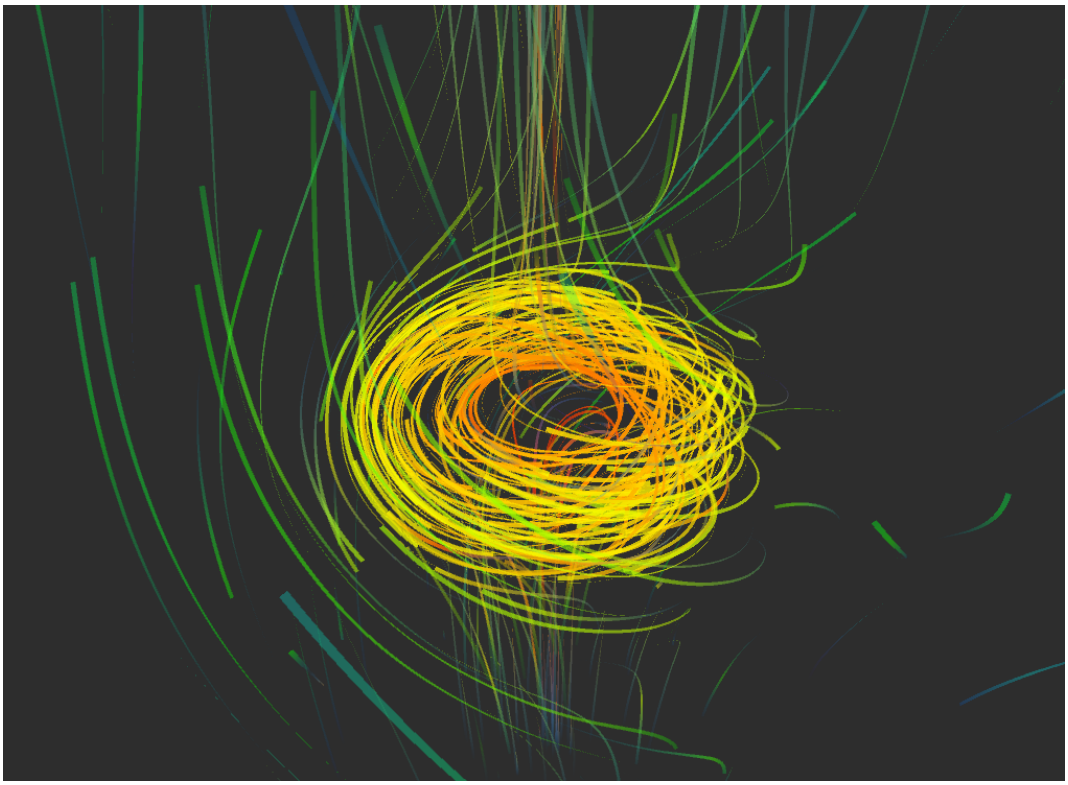

FIG. 12: Hopfion visualized using tracer method that was developed in this work. In the interactive animation the camera can be swiveled around the center of the object to obtain a 3D understanding of the field.

When the tracers method is expanded into 3D it starts to become a bit messy again. This was mitigated by adding an interactive component. The option to orbit the camera around the center of the visualization is added. This allows the depth of the tracers to be easily seen as it shows different perspectives. An example of this approach can be seen displaying a Hopfion in FIG. 12. It highlights areas of interest as can be seen at the center of the field. The tracers concentrate there and expose the behavior at the center, this is convenient as the field becomes far less interesting further out.

We put few months' work into expanding this tracer method to 3D. The goal was for it to be used to visualize the minimized energy field. This work was done in Unity with C# and a completed working visualization system was created. However, it failed to capture any new information about our field. Though, it was successful in other cases, such as with the Hopfion in FIG. 12.

A large issue with the tracer method (especially in our case) is discontinuous fields. Here the question becomes what to do with the tracer when it hits such a discontinuity. The first approach is to let the tracer continue on moving with its previous direction and velocity, however this hides the fact that discontinuity is there as its space is still filled by tracers. The second is stop the tracer when it hits the surface, letting its tail die out. The issue here is that this destroys the tails of the tracers in tight sections (like the center of the torus). It is the moving trails that make this method stand out and the discontinuity of the field ruins that.

In the end the tracer method did not provide any more insight to our field configuration than the more standard plots did. Finding a good visualization method is an open-ended process and will always need to be tweaked for the specific configuration being studied. Though not helpful for our torus configuration (as it is discontinuous), elements of the Hopfion's field were highlighted by this strategy and created some interesting patterns. So, maybe this could prove useful in other continuous field cases as well.

## V. RESULTS AND DISCUSSION

The results that were gathered were the minimum energies with respect to the different tori shapes. This creates a map of minimum energy across tori shape which can be used to determine where a torus would settle (in shape) if it were allowed to morph. The interesting region of this map is around this minimum; thus that region was focused on.

Preliminary runs were made to isolate the location of the minimum. It was known it would be on the order of 1 as it was non-dimensionalized and that is the order on which the standard LC elastic energy term meets the fourth-order energy term (as discussed in the energy scaling discussion at the start of section II D). Once this region was isolated we knew that the scaling discussion was correct in that a minimum existed. A grid of points was evenly spaced across the tori shape space around the minimum. These points are where the simulation was run to create the minimum energy map. This mapping allowed for the curvature of the energy map to be known. From this raw data, the discrete points were fit, and a smooth surface was extrapolated.

The chosen points created a 6x20 grid for $\tau$ by $u$. The six $\tau$ values chosen were 1.1, 1.2, 1.3, 1.4, 1.5, and 1.6 with $u$ linearly spaced between $0.2\,\lambda$ and $0.4\,\lambda$. For each simulation the region was a cube with side lengths of $2\,\lambda$ and a grid size of 111 on each side (approximately equal to a grid width — the width between two adjacent grid points — of $0.018\,\lambda$). The integrals were taken using a further 20 divisions for each discrete cube within the grid. The minimization factor was $\beta = 0.005$.

As the torus becomes small or large relative to the grid resolution of the system more computational noise starts to appear in the simulation (as seen in the raw data points of FIG. 13). This is due to the quantization and coarse nature of the grid. When the torus is small relative to the grid the smallest possible change still produces a large step in the volume of the torus.

This noise is handled by fitting a quadratic curve to each constant $\tau$ line — an example fitting can be seen in FIG. 13. The final result of all of the fits is displayed in FIG. 14.

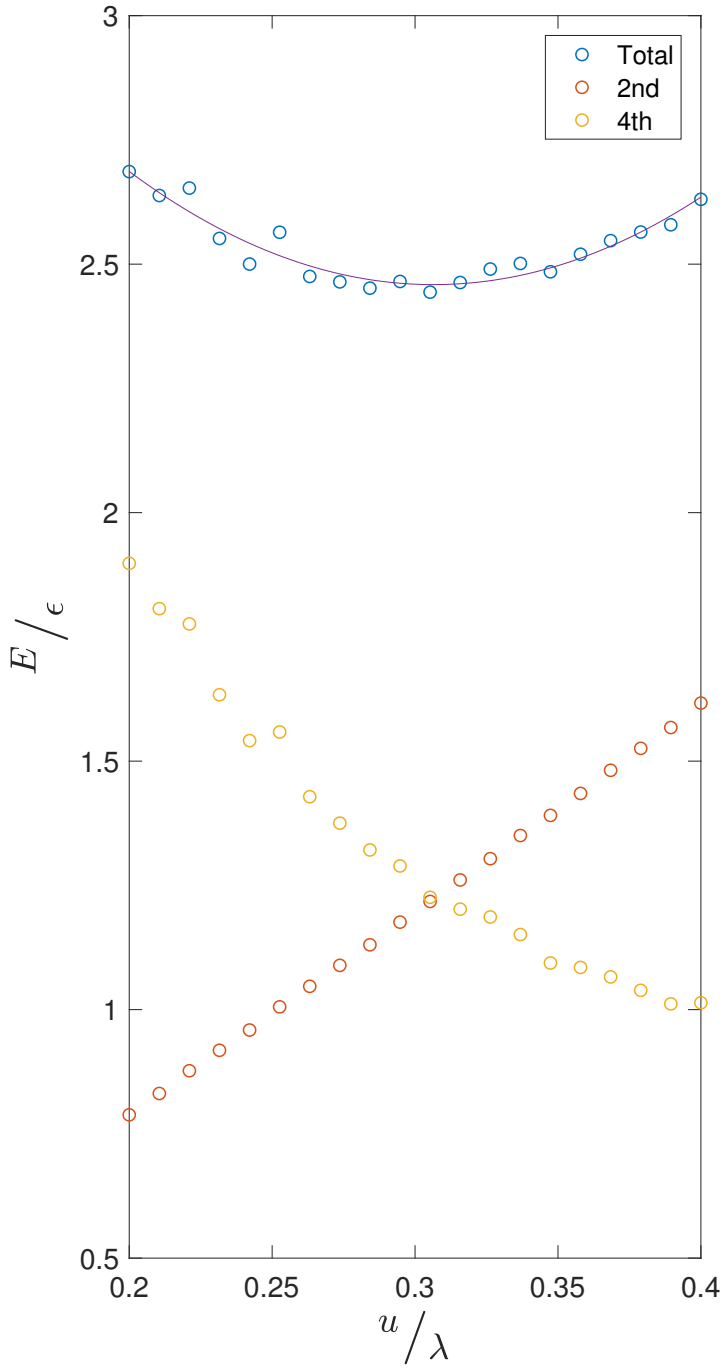


FIG. 13: Minimum energy data with fit, $\tau = 1.4$. The orange circles represent the values for the 2nd order part of the energy, the yellow circles represent the values for the 4th order part of the energy, and the blue circles (and purple line) show the total energy (e.g. the sum of the second and fourth). For each value of $u$ (with constant $\tau$) the torus configuration was minimized, and the final energy recorded. The raw data from the simulation had some noise (blue dots), as the torus gets smaller, $u \to 0$, relative to the fixed grid size the average error of the points increases (more noise). However, as the torus gets larger with respect to the grid, $u \to \infty$, the average error of the points decreases (less noise). To clean this noise up it is fitted to a quadratic curve (the purple line).

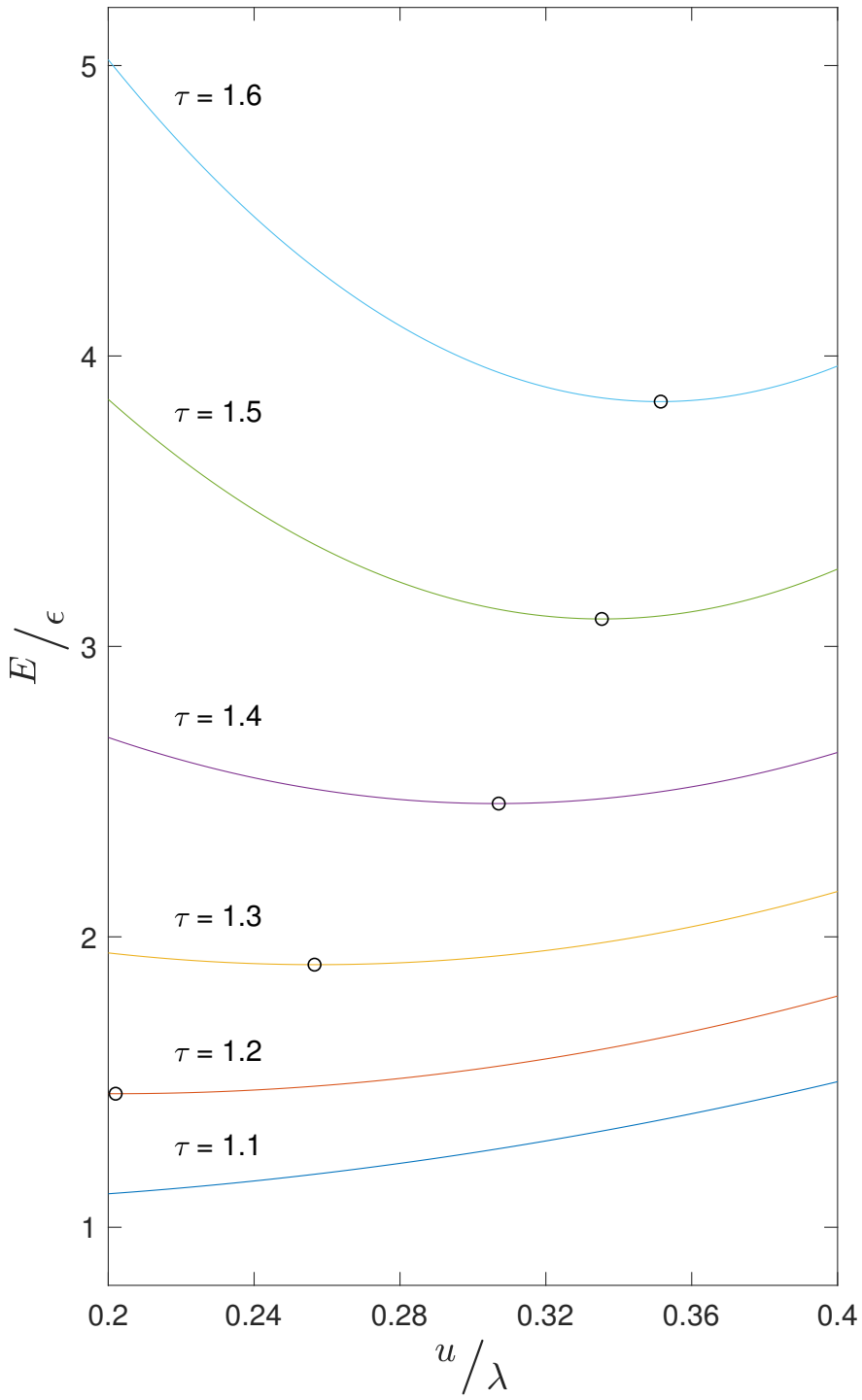


FIG. 14: Minimum energy fit lines for constant $\tau$. All $\tau$'s are fit and plotted together to see that then minimum energy decreases for all u, as $\tau$ decreases. The constant $\tau$ lines also show that there is a minimum u for each $\tau$, represented by the black circles. The $\tau = 1.1$ line theoretically has a minimum as well, however it is not within the sampled space.

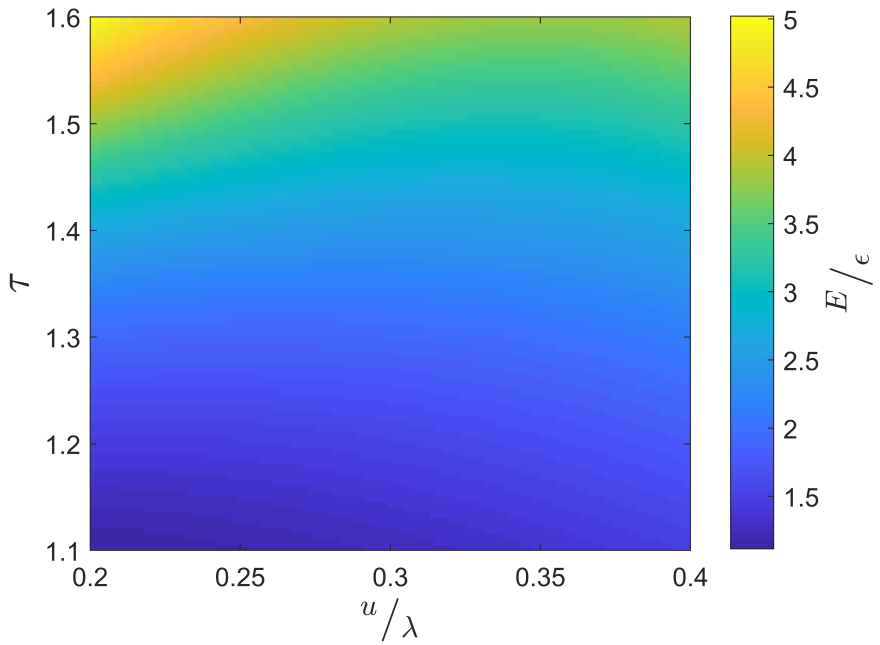


FIG. 15: Energy map across torus shape. This shows how the minimum energy of the torus changes as the shape changes. In general, as $\tau$ increases so does the energy. $u$ has some clear minimum points to the top, these continue downwards but become harder to distinguish.

A clear progression of energy minimization as $\tau$ decreases becomes apparent once all the $\tau$ lines are displayed together. For each $\tau$ it is also clear that there is a minimum energy along $u$, this shows that the additional fourth-order energy term did its job. The final key point in FIG. 14 is that as $\tau$ decreases the minimum $u$ decreases as well.

The next step of the fitting of the data was to interpolate between the different $\tau$ values. This was required to create a smooth surface over the region. A *spline* interpolation method was used on the fitted data. This created the energy color map and the energy contour map in FIG. 15 and FIG. 16 respectively.

The energy color map produced from the fitting and interpolation of the data in FIG. 15 clearly shows that the global minimum energy point trends towards $\tau = 0$ and $u = 0$. If the meanings of these toroidal coordinates are thought about this trend becomes clear. As $\tau$ decreases the width of the torus tube increases (as seen in 6) consuming continuously more of the field — as anything parts of the field inside of the torus don't exist. Then when the

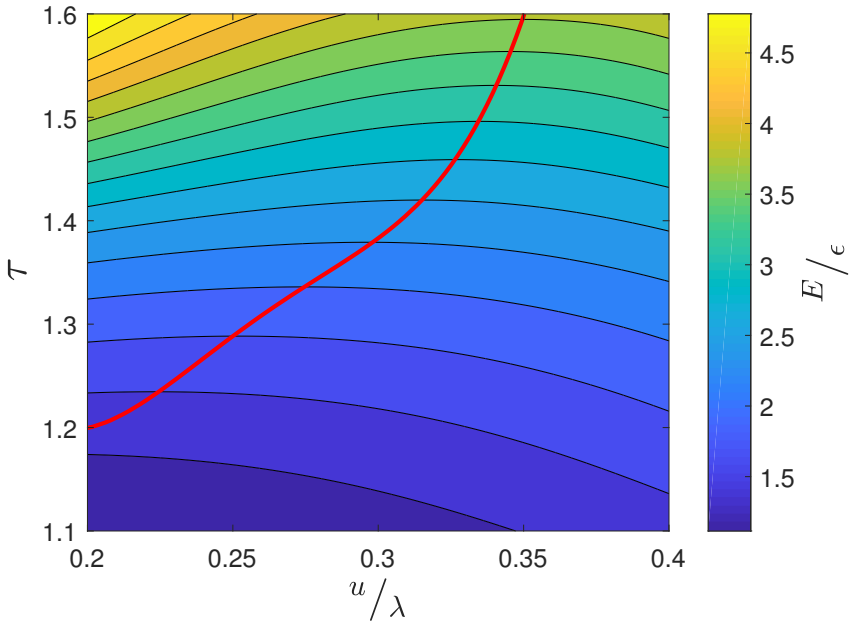


FIG. 16: Energy contour map across torus shape with minimum energy line. This graph highlights the constant energy lines (the contours) of the minimum energy with respect to the torus shape. The red line shows the minimum energy points along $u$ for constant $\tau$ — it follows the peaks of the constant energy contours, the gradient of the energy surface.

energy is calculated there is less field to sum over and thus the energy is lower. And as $u$ decreases the inner radius of the torus decreases. So, as both of these values shrink together the field becomes completely consumed. This leaves the field with no parts that hold energy and thus the total energy is zero.

Contour lines are added to the energy color map in FIG. 16. These lines show constant energy values. It is not a coincidence that the minimum energy line meets the peaks of each of these contours. As the contours decrease in energy as $\tau$ decreases for a constant $\tau$ the minimum energy will be the single point of that minimum energy that reaches up to that $\tau$. This clearly demonstrates that the minimum energy is the gradient of the energy surface. Any torus that was allowed to morph would slowly converge towards this minimum energy line as they explode in size.

Both FIG. 15 and FIG. 16 illustrate that the fourth-order term did its job in stabilizing the shrinking along $u$. However, the configuration is still unstable along $\tau$ as there is nothing stopping the torus from continually expanding it will do so until there is no field left. Thus,

there is a tendency for the torus to expand, expelling the field from the computational domain. This can be balanced by introducing an external "pressure" term that will force it to shrink again. This has not been done in this work.

## VI. SUMMARY AND CONCLUSIONS

Throughout this thesis I studied liquid crystal theory, starting at 2D and working through 3D to the tensor model with an additional fourth-order term. The simulation code followed this same process as each step was used to help verify the next. The code went through a few methods, first parameterizing the field as an angle (for 2D) and then moving onto the Lagrange multipliers method with the molecular field for three dimensions.

Different visualization techniques were also used to help validate the simulations. For the 2D case this mostly consisted of quiver plots as they were sufficient for that simplicity of the system. As we moved onto 3D we started developing the more complex visualization experiments discussed in section IV. At this point the simulation development and visualization development diverged a bit. However, in the end the visualization method was brought back around to try with the fully minimized torus field.

The simulation was rigorously tested along the way including comparing its results to another simulation that was developed independently for the purpose of debugging. Along with this were the many theory confirmations that were mentioned throughout sections II and III.

The minimization code successfully minimized a $\pi$-twist finding a stable energy. So, for different initial configurations of a $\pi$-twist different finite minimum energy values could be found. This was even true before the fourth-order term was added. The fourth-order term stabilized the size of the torus in one dimension. This shows that the $\pi$-twist defect is theoretically possible in standard LCs with stable torus boundaries.

As seen in the energy maps (FIG. 15 and FIG. 16) the minimum energy of the torus was found for constant $\tau$. This means that the fourth-order energy term did its job of opposing the standard elastic energy of the LCs when the torus was small. However, as was seen the torus does not have a (non-zero) global minimum under the current model. This is because there is nothing preventing the torus from expanding to an infinite size. As this could never happen in a real LC there must be a volume "pressure" term that is missing from the model.

This term would push against the growth of the torus providing stabilization in size. With this added the $\pi$-twist defect would be stable in both energy and size, leading to a global minimum (e.g. the defect could exist in the field without any additional support).

Once a global minimum is found for the $\pi$-twist defect other interesting questions appear. What would happen if there were more than one torus in the system? Potentially, the relative chirality (i.e. the direction the $\pi$-twist is twisted) between each of the twists could affect their behavior on each other. This relative chirality could potentially create a push and a pull effect (on two tori) that is similar to electric charges. Also, the energy would now (potentially) be dependent upon the relative angle between the tori. Having more than one torus in the system would allow for a large amount of new behavior to emerge.

Another avenue to explore is to see if more complex objects are stable within this energy model. For example, objects with twists around knotted lines. These situations are where advanced visualization techniques begin to make a large difference. These objects would be vastly more complicated than the torus and would be much harder to understand and visualize through text or imagination.

**ACKNOWLEDGMENTS**

I would like to thank my advisor Pavel Kornilovich. He provided me with the knowledge and guidance to complete this research and thesis. I would also like to thank Ethan Minot for providing feedback and ideas on my thesis during the writing process. Finally, I would like to thank Stephanie Egger for being so supportive and dealing with me when I was frustrated with code.

---

[1] Manuel Asorey, "Space, matter and topology," Nature Physics **12**, 616618 (2016).

[2] N. D. Mermin, "The topological theory of defects in ordered media," Reviews of Modern Physics **51**, 591648 (1979).

[3] "The nobel prize in physics 2016," https://www.nobelprize.org/prizes/physics/2016/summary/ (2016).

[4] Pierre-Gilles de Gennes and Jacques Prost, *The Physics of Liquid Crystals* (Oxford University Press, 1993).

[5] Paul J. Ackerman and Ivan I. Smalyukh, "Reversal of helicoidal twist handedness near point defects of confined chiral liquid crystals," Physical Review E **93** (2016), 10.1103/physreve.93.052702.

[6] Paul J. Ackerman and Ivan I. Smalyukh, "Diversity of knot solitons in liquid crystals manifested by linking of preimages in torons and hopfions," Physical Review X **7** (2017), 10.1103/physrevx.7.011006.

[7] "Upward spiral arrow," https://thenounproject.com/term/upward-spiral/184499/ .

[8] "Torus shape," https://www.kisspng.com/png-torus-shape-of-the-universe-topology-geometry-vort-1814495 .

[9] Houjie Tu, Gerhard Goldbeck-Wood, and Alan H. Windle, "Deterministic numerical model for treating the three elastic constants in nematic liquid-crystalline polymers," Physical Review E **64** (2001), 10.1103/physreve.64.011704.

[10] J. Larmor, *Aether and Matter* (Cambridge University Press, 1900).

[11] A. Unzicker, "What can physics learn from continuous mechanics?" (2000), arXiv:gr-qc/0011064.

[12] T. H. R. Skyrme, "A non-linear field theory," Proceedings of the Royal Society of London. Series A. Mathematical and Physical Sciences **260**, 127138 (1961).

[13] V. E. Korepin and L. D. Faddeev, "Quantization of solitons," Theoretical and Mathematical Physics **25**, 10391049 (1975).

[14] L. Faddeev and Antti J. Niemi, "Stable knot-like structures in classical field theory," Nature **387**, 5861 (1997).

[15] Cameron Beccario, "A global map of wind, weather, and ocean conditions," https://earth.nullschool.net/ .

## Appendix A: Frank-Oseen energy density

### 1. One-constant approximation

When simplifying (1) using (16) the $K_1$ term does not reduce; therefore only the $K_2$ and $K_3$ vector terms are considered. Start by expanding their common vector term in components,

$$\nabla \times \mathbf{n} = \left(\frac{\partial n_z}{\partial y} - \frac{\partial n_y}{\partial z}\right)\hat{\mathbf{i}} - \left(\frac{\partial n_z}{\partial x} - \frac{\partial n_x}{\partial z}\right)\hat{\mathbf{j}} + \left(\frac{\partial n_y}{\partial x} - \frac{\partial n_x}{\partial y}\right)\hat{\mathbf{k}}\,. \tag{A1}$$

The following substitutions will be made for convenience:

$$a = \frac{\partial n_z}{\partial y} - \frac{\partial n_y}{\partial z}\ ,\ b = \frac{\partial n_z}{\partial x} - \frac{\partial n_x}{\partial z}\ ,\ c = \frac{\partial n_y}{\partial x} - \frac{\partial n_x}{\partial y}\,. \tag{A2}$$

Before being squared $K_2$'s and $K_3$'s vector components expand to:

$$\mathbf{n}\cdot[\nabla\times\mathbf{n}] = n_x a - n_y b + n_z c\,, \tag{A3}$$

$$\mathbf{n}\times[\nabla\times\mathbf{n}] = (n_y c + n_z b)\,\hat{\mathbf{i}} - (n_x c - n_z a)\,\hat{\mathbf{j}} - (n_x b + n_y a)\,\hat{\mathbf{k}}\,. \tag{A4}$$

The $K_2$ and $K_3$ portion of (1) can be simplified using (16) to

$$\begin{aligned} f - f_{K_1} &= \frac{1}{2}K_2\left(\mathbf{n}\cdot[\nabla\times\mathbf{n}]\right)^2 + \frac{1}{2}K_3\left[\mathbf{n}\times[\nabla\times\mathbf{n}]\right]^2 \\ &= \frac{1}{2}K\left(\left(\mathbf{n}\cdot[\nabla\times\mathbf{n}]\right)^2 + \left[\mathbf{n}\times[\nabla\times\mathbf{n}]\right]^2\right), \end{aligned} \tag{A5}$$

where $f_{K_1} = \frac{1}{2}K_1\left(\nabla\mathbf{n}\right)^2$. (A3) and (A4) can be squared, plugged into (A5), and simplified,

$$\begin{aligned} f - f_{K_1} = \frac{1}{2}K\Big\{ &\Big[\ (n_x a)^2 - \cancel{2(n_x a)(n_y b)} + (n_y b)^2 + \cancel{2(n_x a)(n_z c)} + (n_z c)^2 - \cancel{2(n_y b)(n_z c)}\Big] \\ &+ \Big[\ (n_y c)^2 + \cancel{2(n_y c)(n_z b)} + (n_z b)^2 + (n_x c)^2 - \cancel{2(n_x c)(n_z a)} + (n_z a)^2 \\ &\quad + (n_x b)^2 + \cancel{2(n_x b)(n_y a)} + (n_y a)^2\Big]\Big\}\,. \end{aligned} \tag{A6}$$

Finally, using the unit length constraint $\mathbf{n}^2 = 1$ (A6) simplifies to,

$$\begin{aligned} f - f_{K_1} &= \frac{1}{2} K \left\{ (a^2 + b^2 + c^2) \cancel{(n_x^2 + n_y^2 + n_z^2)} \right\} \\ &= \frac{1}{2} K \left\{ (\nabla \times \mathbf{n})^2 ) \right\} . \end{aligned} \tag{A7}$$

Now (A7) can be solved for $f$, relabeling $f \to f_0$ to denote the one-constant approximation, and $K_1$ can be replaced with $K$ in accordance with (16) leaving (17).

### 2. Derivation of (18)

Consider an alternative form of (17),

$$\tilde{f}_0 = \frac{1}{2} K \sum_{i,j=1}^{3} \left( \frac{\partial n_i}{\partial r_j} \right)^2 . \tag{A8}$$

Expanding (17) and (A8) into components respectfully yields:

$$\begin{aligned} f_0 = \frac{1}{2} K \Bigg\{ & \left[ \frac{\partial n_x}{\partial x}^2 + 2 \frac{\partial n_x}{\partial x} \frac{\partial n_y}{\partial y} + 2 \frac{\partial n_x}{\partial x} \frac{\partial n_z}{\partial z} + \frac{\partial n_y}{\partial y}^2 + 2 \frac{\partial n_y}{\partial y} \frac{\partial n_z}{\partial z} + \frac{\partial n_z}{\partial z}^2 \right] + \\ & + \left[ \frac{\partial n_z}{\partial y}^2 - 2 \frac{\partial n_z}{\partial y} \frac{\partial n_y}{\partial z} + \frac{\partial n_y}{\partial z}^2 + \frac{\partial n_z}{\partial x}^2 - 2 \frac{\partial n_z}{\partial x} \frac{\partial n_x}{\partial z} + \frac{\partial n_x}{\partial z}^2 + \right. \\ & \left. + \quad \frac{\partial n_y}{\partial x}^2 - 2 \frac{\partial n_y}{\partial x} \frac{\partial n_x}{\partial y} + \frac{\partial n_x}{\partial y}^2 \right] \Bigg\} , \end{aligned} \tag{A9}$$

$$\begin{aligned} \tilde{f}_0 = \frac{1}{2} K \Bigg\{ & \frac{\partial n_x}{\partial x}^2 + \frac{\partial n_x}{\partial y}^2 + \frac{\partial n_x}{\partial z}^2 + \frac{\partial n_y}{\partial x}^2 + \frac{\partial n_y}{\partial y}^2 + \\ & + \frac{\partial n_y}{\partial z}^2 + \frac{\partial n_z}{\partial x}^2 + \frac{\partial n_z}{\partial y}^2 + \frac{\partial n_z}{\partial z}^2 \Bigg\} . \end{aligned} \tag{A10}$$

Compare the two functions' difference of the total energy,

$$\begin{aligned} F_0 - \tilde{F}_0 &= \int \mathrm{d}^3\mathbf{r}\,\{f_0 - \tilde{f}_0\} \\ &= K\int \mathrm{d}^3\mathbf{r}\left\{\left[\frac{\partial n_x}{\partial x}\frac{\partial n_y}{\partial y} - \frac{\partial n_x}{\partial y}\frac{\partial n_y}{\partial x}\right] + \left[\frac{\partial n_z}{\partial z}\frac{\partial n_x}{\partial x} - \frac{\partial n_z}{\partial x}\frac{\partial n_x}{\partial z}\right] + \right. \\ &\left. + \left[\frac{\partial n_y}{\partial y}\frac{\partial n_z}{\partial z} - \frac{\partial n_y}{\partial z}\frac{\partial n_z}{\partial y}\right]\right\}. \end{aligned} \tag{A11}$$

Strategic integration by parts can be performed to create further cancellations,

$$\begin{aligned} F_0 - \tilde{F}_0 = K\Bigg\{ &\left[\left(n_x\frac{\partial n_y}{\partial y} - \cancel{\int \mathrm{d}^3\mathbf{r}\left\{n_x\frac{\partial^2 n_y}{\partial x\partial y}\right\}}\right) - \left(n_x\frac{\partial n_y}{\partial x} - \cancel{\int \mathrm{d}^3\mathbf{r}\left\{n_x\frac{\partial^2 n_y}{\partial y\partial x}\right\}}\right)\right] \\ &+ \left[\left(n_z\frac{\partial n_x}{\partial x} - \cancel{\int \mathrm{d}^3\mathbf{r}\left\{n_z\frac{\partial^2 n_x}{\partial z\partial x}\right\}}\right) - \left(n_z\frac{\partial n_x}{\partial z} - \cancel{\int \mathrm{d}^3\mathbf{r}\left\{n_x\frac{\partial^2 n_x}{\partial x\partial z}\right\}}\right)\right] \\ &+ \left[\left(n_y\frac{\partial n_z}{\partial z} - \cancel{\int \mathrm{d}^3\mathbf{r}\left\{n_y\frac{\partial^2 n_z}{\partial y\partial z}\right\}}\right) - \left(n_y\frac{\partial n_z}{\partial y} - \cancel{\int \mathrm{d}^3\mathbf{r}\left\{n_y\frac{\partial^2 n_z}{\partial z\partial y}\right\}}\right)\right]\Bigg\}. \end{aligned} \tag{A12}$$

These cancellations can be made because the mixed partial derivatives are equal. What is left in (A12) after the mixed partials are canceled is only the surface terms of the energy. These can be discarded as during the simulation these will be fixed by being manually set. So, (A8) is equal to (17) up to the surface terms.

## Appendix B: Tensor model of LC distortion energy

This derivation follows that of Tu et al [9].

### 1. Energy density of tensor model

First, assume (27) and expand $Q_{jk}$,

$$f_T = \frac{1}{4}K\left[\nabla_i\left(n_jn_k - \frac{1}{3}\,\delta_{jk}\right)\nabla_i\left(n_jn_k - \frac{1}{3}\,\delta_{jk}\right)\right]. \tag{B1}$$

The derivatives can be applied and the resultant square can be expanded,

$$\begin{aligned} f_T &= \frac{1}{4}K\Big\{(\nabla_i n_j)n_k + n_j(\nabla_i n_k)\Big\}^2 \\ &= \frac{1}{4}K\Big\{(\nabla_i n_j)^2 n_k n_k + (\nabla_i n_j)n_k n_j(\nabla_i n_k) + \\ &\qquad + n_j(\nabla_i n_k)(\nabla_i n_j)n_k + n_j n_j(\nabla_i n_k)^2\Big\}\,. \end{aligned} \tag{B2}$$

Due to the unit length constraint, $n_i n_i = n_x^2 + n_y^2 + n_z^2 = \mathbf{n}^2 = 1$. So, (B2) can be reduced to

$$f_T = \frac{1}{4}K\{(\nabla_i n_j)^2 + (\nabla_i n_k)^2 + 2(\nabla_i n_j)n_j(\nabla_i n_k)n_k\}\,, \tag{B3}$$

where the two middle terms are equal as the indices are arbitrary. Finally, notice

$$\nabla_i(n_j n_j) = 2(\nabla_i n_j)n_j = \nabla_i(1) = 0\,, \tag{B4}$$

which allows (B3) to be reduced further to

$$f_T = \frac{1}{4}K\{(\nabla_i n_j)^2 + (\nabla_i n_k)^2\} = \frac{1}{2}K(\nabla_i n_j)^2\,. \tag{B5}$$

This is equivalent to (18).

### 2. Molecular field of tensor model

Starting with $f_T$ from (27) a small variation $\delta Q_{jk}$ can be applied at all points of its total energy, $F_T\left[Q_{jk}\right] \to F_T\left[Q_{jk} + \delta Q_{jk}\right]$. The varied $F_T$ can be expanded to,

$$F_T\left[Q_{jk} + \delta Q_{jk}\right] = \int d^3\mathbf{r}\{f_T(Q_{jk} + \delta Q_{jk}, \nabla_i Q_{jk} + \delta\nabla_i Q_{jk})\}\,. \tag{B6}$$

Then integration by parts can be performed,

$$\delta F_T\left[Q_{jk}\right] = F\left[Q_{jk} + \delta Q_{jk}\right] - F\left[Q_{jk}\right] = \int d^3\mathbf{r}\left\{\frac{\partial f_T}{\partial Q_{jk}} - \nabla_i\left(\frac{\partial f_T}{\partial \nabla_i Q_{jk}}\right)\right\}\,. \tag{B7}$$

In (27) it can be noticed that the energy only depends on $\nabla_i Q_{jk}$. Thus, the first partial derivative in (B7) is zero. Leaving the second equal to,

$$\frac{\partial f_T}{\partial(\nabla_i Q_{jk})} = \frac{K}{2}\nabla_i Q_{jk} \tag{B8}$$

as given by (27). This reduces (B7) to

$$\delta F_T = -\frac{K}{2}\int d^3\mathbf{r}\left\{(\nabla_i\nabla_i Q_{jk})\,\delta Q_{jk}\right\} . \tag{B9}$$

Next, the definition of $Q_{jk}$ can be used to root the equation back in $\mathbf{n}$,

$$\delta Q_{jk} = \delta\left(n_j n_k - \frac{1}{3}\delta_{jk}\right) = n_j\delta n_k + n_k\delta n_j . \tag{B10}$$

Then using $Q_{jk} = Q_{kj}$ the indices $j$ and $k$ can be exchanged leading to,

$$\delta Q_{jk} = 2n_j\delta n_k . \tag{B11}$$

This can be applied to (B9) to find $\delta F_T$ with respect to $\mathbf{n}$,

$$\delta F = -K\int d^3\mathbf{r}\,(\nabla_i\nabla_i Q_{jk})\,n_j\delta n_k . \tag{B12}$$

By comparing (B9), (B12), and (11) the molecular field for the tensor model is found,

$$h_k = K n_j\nabla_i\nabla_i Q_{jk} . \tag{B13}$$

This completes the derivation for (28).

**Appendix C: Energy invariance with respect to global rotation**

A vector rotation in three dimensions are described by 3x3 orthogonal matrices $A_{kq}$. The vector components are transformed as,

$$n'_k = A_{kq} n_q \, . \tag{C1}$$

The property of orthogonality means (summation assumed),

$$A_{kq} A_{kp} = \delta_{qp} \, . \tag{C2}$$

$$A_{kq} A_{pq} = \delta_{kp} \, . \tag{C3}$$

Global rotations implies that matrix $A_{kq}$ is independent of coordinates $x_i$:

$$\nabla_i A_{kq} = 0 \, . \tag{C4}$$

Substituting (C1) into (27) one obtains a "rotated" energy density

$$\begin{aligned}
\frac{4}{K} \tilde{f}'_T &= \left(\nabla_i n'_j n'_k\right) \left(\nabla_i n'_j n'_k\right) \\
&= \left(\nabla_i A_{jp} n_p A_{kq} n_p\right) \left(\nabla_i A_{ja} n_a A_{kb} n_b\right) \\
&= \left(\nabla_i n_p n_q\right) \left(\nabla_i n_a n_b\right) A_{jp} A_{ja} A_{kq} A_{kb} \\
&= \left(\nabla_i n_p n_q\right) \left(\nabla_i n_a n_b\right) \delta_{pa} \delta_{qb} \\
&= \left(\nabla_i n_p n_q\right) \left(\nabla_i n_p n_q\right) \\
&= \left(\nabla_i Q_{pq}\right) \left(\nabla_i Q_{pq}\right) = \frac{4}{K} \tilde{f}_T
\end{aligned} \tag{C5}$$

This shows that the "rotated" energy is the same as the original energy.